Monthly Notices
of the
ROYAL ASTRONOMICAL SOCIETY

MNRAS **486,** 1882–1906 (2019)
Advance Access publication 2019 March 29

doi:10.1093/mnras/stz838

Lyα emitters in a cosmological volume – I. The impact of radiative transfer

Siddhartha Gurung-López,[1]★ Álvaro A. Orsi,[1] Silvia Bonoli,[1] Carlton M. Baugh[2] and Cedric G. Lacey[2]

[1]*Centro de Estudios de Física del Cosmos de Aragón, Plaza San Juan 1, piso 2, Teruel, E-44001, Spain*
[2]*Institute for Computational Cosmology, Department of Physics, Durham University, Science Laboratories, South Road, Durham DH1 3LE, UK*

Accepted 2019 March 19. Received 2019 March 9; in original form 2018 June 29

ABSTRACT

Lyman-α emitters (LAEs) are a promising target to probe the large-scale structure of the Universe at high redshifts, $z \gtrsim 2$. However, their detection is sensitive to radiative transfer effects that depend on local astrophysical conditions. Thus, modeling the bulk properties of this galaxy population remains challenging for theoretical models. Here we develop a physically motivated scheme to predict LAEs in cosmological simulations. The escape of Lyα photons is computed using a Monte Carlo radiative transfer code that outputs a Lyα escape fraction. To speed up the process of assigning escape fractions to individual galaxies, we employ fitting formulae that approximate the full Monte Carlo results within an accuracy of 10 per cent for a broad range of column densities, gas metallicities, and gas bulk velocities. We apply our methodology to the semi-analytical model `galform` on a large *N*-body simulation. The Lyα photons escape through an outflowing neutral gas medium, implemented assuming different geometries. This results in different predictions for the typical column density and outflow velocities of the LAE population. To understand the impact of radiative transfer on our predictions, we contrast our models against a simple abundance matching assignment. Our full models populate LAEs in less massive haloes than what is obtained with abundance matching. Overall, radiative transfer effects result in better agreement when confronting the properties of LAEs against observational measurements. This suggests that incorporating the effects of Lyα radiative transfer in the analysis of this galaxy population, including their clustering, can be important for obtaining an unbiased interpretation of future data sets.

Key words: Radiative transfer – ISM: jets and outflows – Galaxy: evolution.

1 INTRODUCTION

During the past two decades, surveys targeting the Lyα emission in star-forming galaxies, the so-called Lyα emitters (LAEs), have detected objects out to redshift $z \sim 7$ (e.g. Steidel et al. 1996; Hu, Cowie & McMahon 1998; Rhoads et al. 2000; Malhotra & Rhoads 2002; Taniguchi et al. 2005; Kashikawa et al. 2006; Guaita et al. 2010; Konno et al. 2016; Sobral et al. 2017). The study of this galaxy population has allowed us to explore the kinematics of the interstellar medium (ISM) in high redshift galaxies (Shapley et al. 2003; Steidel et al. 2010, 2011; Kulas et al. 2011; Chisholm et al. 2017; Guaita et al. 2017), the large-scale structure (Gawiser et al. 2007; Orsi et al. 2008; Ouchi et al. 2010; Bielby et al. 2016; Kusakabe et al. 2018; Ouchi et al. 2018), the epoch of re-ionization (Santos et al. 2004; Kashikawa et al. 2006; Dayal, Maselli & Ferrara 2011; Inoue et al. 2018) and to test galaxy formation models (Le Delliou et al. 2006; Kobayashi, Totani & Nagashima 2007; Nagamine et al. 2010; Orsi, Lacey & Baugh 2012).

Despite the success in detecting progressively larger samples of LAEs, their physical interpretation has proven to be a difficult challenge (see Dijkstra 2017, for a review). Lyα photons are easily scattered by neutral hydrogen, causing a large increase in the path that the photon needs to travel through neutral hydrogen clouds (e.g. Harrington 1973; Neufeld 1990). This results in an increased probability of interaction with dust grains, and thus, absorption. Hence, the Lyα radiative transfer through a neutral medium reduces the Lyα flux that escapes the galaxy and also modifies the line profile, since each scattering event changes the frequency of the photons. These physical processes also take place in the surrounding intergalactic medium (IGM) of galaxies and can also modify the observed Lyα flux and line profile (Santos et al. 2004; Dijkstra, Mesinger & Wyithe 2011).

★ E-mail: sidgurung@cefca.es

Analytical approximations for Lyα radiative transfer have been derived for oversimplistic neutral gas configurations (e.g. Harrington 1973; Neufeld 1990; Dijkstra, Haiman & Spaans 2006). More realistic configurations can be explored with a Monte Carlo algorithm. Individual Lyα photons are generated inside a neutral hydrogen cloud with a given geometry, kinematics, and temperature. The path of Lyα photons is tracked, including their interactions, which produce scattering events, until the photons escape or are absorbed by dust. This approach has been studied in several scenarios (Ahn, Lee & Lee 2000; Zheng & Miralda-Escudé 2002; Ahn 2003; Verhamme, Schaerer & Maselli 2006; Gronke et al. 2016). Most notably, the Monte Carlo radiative transfer has shown to reproduce the diversity of observed Lyα line profiles by allowing photons to escape through an outflowing medium (e.g. Schaerer & Verhamme 2008; Orsi et al. 2012).

Theoretical models of galaxy formation have introduced the effect of radiative transfer in different approximate ways to predict the properties of the LAE population. The first model of LAEs in a hierarchical galaxy formation framework implemented a constant escape fraction of Lyα photons to reproduce their observed abundance and clustering (Le Delliou et al. 2005, 2006; Orsi et al. 2008). Further attempts introduced radiative transfer effects over simple geometries in semi-analytical models (Garel et al. 2012; Orsi et al. 2012). Cosmological hydrodynamical simulations also incorporated Lyα radiative transfer in post-processing. One approach has been to track Lyα rays to simulate different lines of sight (e.g. Laursen & Sommer-Larsen 2007; Laursen, Razoumov & Sommer-Larsen 2009; Laursen, Sommer-Larsen & Razoumov 2011) over small volumes. With a Monte Carlo radiative transfer code, Zheng et al. (2010) showed that the proper treatment of Lyα photons radiative transfer has dramatic effects on the clustering of LAEs. However, recently, Behrens et al. (2017) found no significant change in the clustering of LAEs after implementing Lyα radiative transfer in the Illustris simulation (Nelson et al. 2015), and attribute the claims of Zheng et al. (2010) about the clustering of LAEs to resolution effects.

In the next years many ground-based large surveys such as HETDEX (Hill et al. 2008), J-PAS (Benitez et al. 2014), and space missions like ATLAS-Probe (Wang et al. 2018) will aim to detect LAEs over large areas to trace the large-scale structure (LSS) at high redshifts. Such measurements could potentially deliver cosmological constraints in redshift ranges well above those currently targeted by Multi-Object Spectroscopic surveys. With progressively larger and more accurate data sets, it becomes crucial to improve our theoretical understanding of galaxies as tracers of the underlying matter distribution (Orsi & Angulo 2018). One of our aims in this work is to understand the impact of radiative transfer effects on clustering measurements.

The model for the Lyα luminosity of star-forming galaxies presented here is based on a fast implementation of a Monte Carlo radiative transfer. To avoid the prohibitively long time that it would take to run a Monte Carlo code over millions of galaxies, we develop fitting formulae that reproduce the full Monte Carlo results accurately. To illustrate the potential of our model, we apply this methodology to the semi-analytic model `galform` run over an *N*-body simulation. This is a first paper in a series that explores the properties of galaxies selected by their Lyα luminosity. Here we focus on the impact of the Lyα RT in defining the properties of the LAE galaxy population. In a forthcoming paper we implement the impact of the intergalactic medium (IGM) and the effects of re-ionization on the LAE population.

The outline of this paper is as follows. In Section 2, we develop fitting formulae to predict the escape fraction of Lyman alpha photons through outflows. In Section 3, we describe our model for LAEs that combines galaxy formation physics and Lyα radiative transfer in addition to the implementation of the Lyα RT in a galaxy formation model is presented. We analyse the LAE population predicted by our model in Section 4. We discuss our results in Section 5. Finally, conclusions and future work are summarized in Section 6.

2 MODEL INGREDIENTS

In this section we describe our model ingredients and the methodology we follow to predict the properties of LAEs in a cosmological simulation.

2.1 Lyα radiative transfer

We track the scattering, absorption, and escape of Lyα photons making use of the Monte Carlo radiative transfer code described in Orsi et al. (2012), which has been made publicly available.[1] This code is similar to others in the literature (e.g. Zheng & Miralda-Escudé 2002; Ahn 2003, 2004; Dijkstra et al. 2006; Verhamme et al. 2006; Laursen & Sommer-Larsen 2007; Barnes & Haehnelt 2010, and references therein). A detailed review of Lyα radiative transfer can be found in Dijkstra (2017). Below we summarize the main features of the Orsi et al. (2012) code that are most relevant to this work.

The code receives as input a configuration of a 3D neutral gas geometry, temperature, expansion velocity $V_{\rm exp}$, neutral hydrogen column density $N_{\rm H}$, and optical depth of dust $\tau_{\rm a}$. In this work we use a monochromatic source of photons, i.e. all photons are generated at Lyman α wavelength, $\lambda_0 = 1215.68$ Å. For a given gas distribution, the code generates a Lyα photon with a random direction and follows its interactions with hydrogen and dust until it either is absorbed by dust or escapes from the neutral gas medium. Every interaction with a hydrogen atom results in a scattering event that changes the direction and frequency of the photon. Interactions with dust, on the other hand, can change the direction of the photon or result in absorption depending on the assumed albedo of the dust grains. The process is repeated for N_p photons, recording in the end the frequency of every photon that escaped and those that were absorbed by dust grains. This allows us to compute the escape fraction $f_{\rm esc}^{\rm Ly\alpha}$ and wavelength distribution (i.e. the Lyα line profile) for every outflow geometry over which both the neutral gas and the dust are distributed. In this work we implemented three different outflow geometries, which are illustrated in Fig. 1.

(i) *Thin shell*. This geometry consists of an expanding isothermal homogeneous spherical shell similar to ones found in literature (e.g. Verhamme et al. 2006; Garel et al. 2012; Orsi et al. 2012) . This spherical shell is thin and can be described by an inner radius and an outer radius, $R_{\rm in}$ and $R_{\rm out,}$ respectively, which satisfy $R_{\rm in}/R_{\rm out} = 0.9$. The shell is expanding outwards, thus it has a radial macroscopic velocity $V_{\rm exp} > 0$. The neutral hydrogen column density is given by

$$N_{\rm H} = \frac{M_{\rm H}}{4\pi m_{\rm H} R_{\rm out}^2}, \quad (1)$$

[1] https://github.com/aaorsi/LyaRT

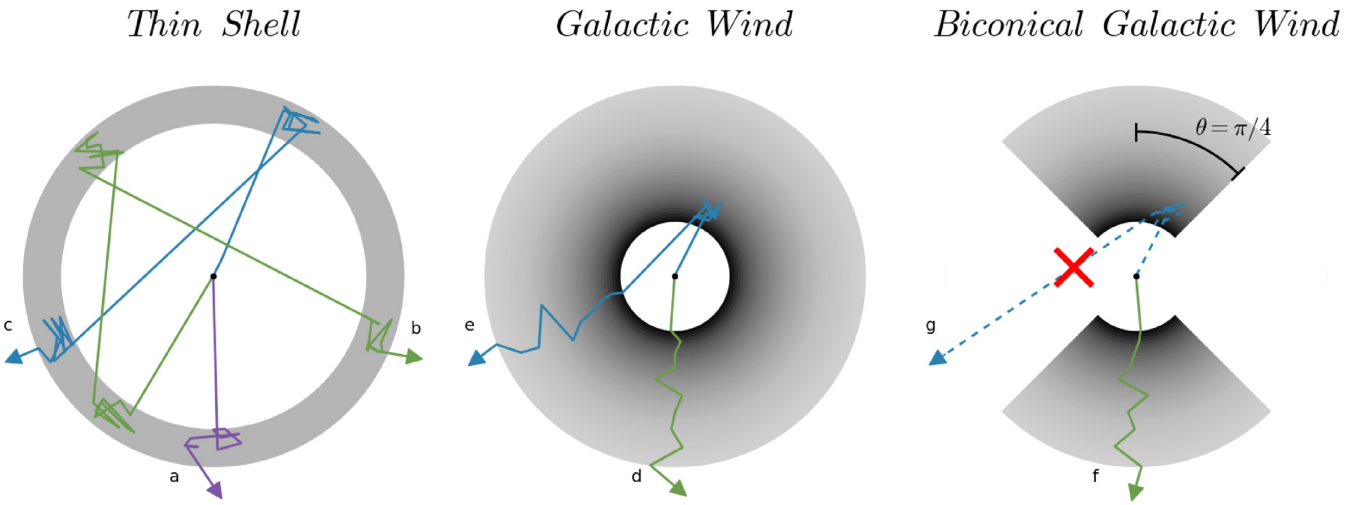

Figure 1. A schematic illustration of the different outflow geometries implemented in this work: *Thin Shell* (left), *Wind* (middle), and *Biconical Wind* (right). The gas density is represented by the grey colour scale. Different possible trajectories of photons are labeled from *a* to *g*. The red cross over photon *g* illustrates the point where this photon is absorbed by the medium.

where $M_{\rm H}$ is the total neutral hydrogen mass and $m_{\rm H}$ is the mass of a hydrogen atom.

The empty cavity in the center of the shell produces photon *backscatterings*, i.e. photons can bounce back into the empty cavity multiple times, as illustrated by photons *b* and *c* in Fig. 1.

(ii) *Galactic wind*. This geometry consists of an expanding spherical gas distribution with a central empty cavity of radius $R_{\rm Wind}$ (Orsi et al. 2012). The gas is isothermal and is expanding radially at a constant velocity $V_{\rm exp}$. Unlike the *Thin Shell*, the gas is distributed with a radial density profile given by:

$$\rho_{\rm H}({\rm r}) = \begin{cases} 0 & r < R_{\rm Wind} \\ \frac{\dot{M}_{\rm H}}{4\pi m_{\rm H} r^2 V_{\rm exp}} & r \geqslant R_{\rm Wind}, \end{cases} \quad (2)$$

where $\dot{M}_{\rm H}$ is the ejection neutral hydrogen mass rate. Thus, the column density in the *Wind* geometry is

$$N_{\rm H} = \frac{\dot{M}_{\rm H}}{4\pi m_{\rm H} R_{\rm Wind} V_{\rm exp}}. \quad (3)$$

This geometry is illustrated in the middle panel of Fig. 1.

We define a large outer radius $R_{\rm out} = 20 R_{\rm Wind,}$ where the computation is forced to end and any photon that have reached this radius is considered to have escaped. We have checked that for greater values of $R_{\rm out}$ the code provides the same line profile and escape fraction. Thus, we conclude that our results converge for our choice of $R_{\rm out}$.

(iii) *Biconical wind*. This geometry shares the same properties of the*Wind*, but additionally it features an aperture angle, $\theta_{\rm cone}$, which defines the volume of gas and dust similar to Zheng & Wallace (2014). In particular, we arbitrarily set $\theta_{\rm cone} = \pi/4$. The resulting polar asymmetry is thus the main difference between the two previous geometries and this one. We checked that there is no strong dependence of $f_{\rm esc}^{{\rm Ly}\alpha}$ with the line of sight (LoS) within the outflow aperture. This geometry is shown in the right-hand panel of Fig. 1.

In the biconical geometry we force photons to be emitted from the centre of the geometry (as in the other geometries) and within the aperture of the bicone, i.e. no photons are emitted outside the bicone. Additionally, due to the empty regions in this geometry, photons that scatter off the internal cavity and escape off the bicone are considered absorbed by the external medium (e.g. photon *g* in Fig. 1). This is equivalent to assuming that there is a dusty optically thick medium surrounding the bicone.

Furthermore, in this geometry we define the escape fraction of Lyα photons as the ratio between the number of photons emitted towards the bicone and the number of photons that escaped through the bicone. This implies that in every galaxy the outflow geometry is pointing towards the observer. We note that the actual fraction of galaxies with a bicone orientated towards the observer would be $\Delta\gamma_b/4\pi$, where $\Delta\gamma_b$ is a solid angle. In fact, if we take into account the galaxy orientation in our models, we find that for the bicone the observed number count of LAEs is too low (as we discuss later). Therefore, our biconical model represents an upper limit. For further details on the bicone implementation, see Appendix A.

Fig. 2 illustrates the difference between the Lyα escape fraction (left-hand panel) and line profile (right-hand panel) predicted by each geometry, for a particular choice of column density and expansion velocity. As expected, the escape fraction decreases towards higher values of $\tau_{\rm a}$ in all geometries, as greater amounts of dust absorb more photons. However, the impact on the geometry of the medium is evident: even if the three configurations have the same $N_{\rm H}$ and $V_{\rm exp}$, photons have the highest escape fractions from the *Wind* geometry and the lowest from the *Bicone*. This is due to the complicated Lyα RT. For example, as in the *Bicone* configuration photons that leak through the empty cavity are considered absorbed, the escape fraction does not reach 1 even if there is no dust in the outflow, making a great difference with respect to the other two geometries. Additionally, even if the *Wind* and *Thin Shell* configurations share spherical symmetry (unlike the *Bicone*) the dependence of $f_{\rm esc}^{{\rm Ly}\alpha}$ on $N_{\rm H}$, $V_{\rm exp}$, and $\tau_{\rm a}$ is different due to the distinctive hydrogen density radial profiles of the two configurations. This dependence on the geometry affects not only the $f_{\rm esc}^{{\rm Ly}\alpha}$ but also the line profile of the Lyα emission. The predicted line shape changes dramatically from a geometry to another: in the case of the *Wind* it is a broad line, for the *Bicone* it is a narrow line, and for the *Thin Shell* it assumes a double-peak profile. We use these three different outflow geometries to

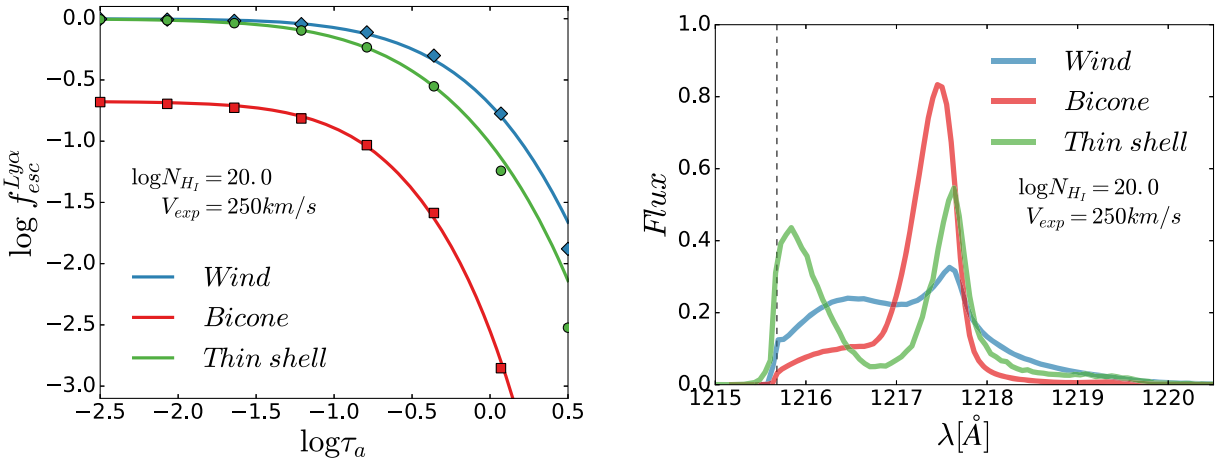

Figure 2. (Left) $f_{\rm esc}^{Ly\alpha}$ versus the dust optical depth $\tau_{\rm a}$ for different geometries in outflows with the same physical properties ($V_{\rm exp}$ and $N_{\rm H}$), as indicated in the figures. The output of the radiative transfer code is represented by green circles, blue diamonds, and red squares for the *Thin Shell*, galactic wind, and biconical geometries, respectively. Additionally, our analytical fit is represented by solid lines with the same colour code as the code's output. (Right) Lyα line profile for different geometries with the same physical properties. In colored lines the radiative transfer code output is plotted for the *Thin Shell* geometry (green), the galactic wind (blue), and the biconical galactic wind (red).

estimate the variance in the LAEs population depending on the geometry.

2.2 Fitting formulae for Lyα radiative transfer

As discussed in Section 2.1, the Monte Carlo radiative transfer code can take a long time to run for a given configuration of parameters. For a single photon, the average number of scatterings, and thus, calculations, grow as a power-law function of the column density of the medium (Harrington 1973). In the parameter space explored here, the completion time of the code can vary from a few seconds up to a few hours in the most extreme cases. Applying this directly in a catalogue of millions of objects would result in prohibitively long execution times.

To overcome this, we develop empirical (measured from the radiative transfer Monte Carlo code) expressions that approximate the results of the Monte Carlo runs. We start by constructing a grid to scan the parameter space with ∼450 configurations spanning the ranges $10 \leq V_{\rm exp}[{\rm km\,s^{-1}}] \leq 1000$ and $-2.5 \leq \log \tau_{\rm a} \leq 0.5$. For the *Thin Shell* and *Wind* geometries we covered $19.0 \leq \log(N_{\rm H}[{\rm cm^{-2}}]) \leq 22.5$. However, due to the excessive computational time in the *Bicone* we restrict our analysis to $19.0 \leq \log(N_{\rm H}[{\rm cm^{-2}}]) \leq 22.0$. We run the Monte Carlo code with 10^4 photons and obtain the Lyα escape fraction, $f_{\rm esc}^{\rm Ly\alpha}$ as a function of $\tau_{\rm a}$, $N_{\rm H,}$ and $V_{\rm exp}$. We set the gas temperature to 10^4 K.

To construct an analytic expression for $f_{\rm esc}^{\rm Ly\alpha}$, we start from a generalized form of the expression for the $f_{\rm esc}^{\rm Ly\alpha}$ in a homogeneous, static slab derived in Neufeld (1990):

$$f_{\rm esc}^{\rm an} = k_3 \left[\cosh \sqrt{k_1 \tau_{\rm a}^{k_2}}\right]^{-1}, \quad (4)$$

where k_1 and k_2 are functions of $N_{\rm H}$ and $V_{\rm exp}$ for all geometries, respectively. Additionally, k_3 is set to 1 in the *Thin Shell* and *Wind* geometries, but is a function, $k_3({\rm N_H}, {\rm V_{exp}}) < 1$, in the *Bicone*, since, in this geometry, the escape fraction is always less than 1 (see Section 2.1). We perform a Monte Carlo Markov Chain (MCMC) with the `emcee`[2] code (Foreman-Mackey et al. 2013a) to determine the functional form of k_1, k_2, and k_3, by minimizing the function

$$\chi^2 = \sum_{\rm N_H, V_{exp}, \tau_a} \left(\frac{f_{\rm esc}^{\rm MC} - f_{\rm esc}^{\rm an}}{\sigma_{\rm MC}}\right)^2, \quad (5)$$

where $f_{\rm esc}^{\rm MC}$ corresponds to the escape fraction of photons obtained with the MC code over each configuration in the grid, and $\sigma_{\rm MC}$ is the error in the calculation of the escape fraction, given by the dispersion in a binomial distribution with probability of success $f_{\rm esc}^{\rm MC}$:

$$\sigma_{\rm MC} = z_{1-\alpha/2}\sqrt{\frac{f_{\rm esc}^{\rm MC}\left(1 - f_{\rm esc}^{\rm MC}\right)}{N}}, \quad (6)$$

where $z_{1-\alpha/2}$ is the $100(1-\alpha/2)$-th percentile of the standard normal distribution. In particular, we use the quantile 95, i.e. $\alpha = 0.1$. Additionally, N is the number of generated photons in each configuration.

The functional form and parameter values of the fits for $k_1(N_{\rm H}, V_{\rm exp})$, $k_2(N_{\rm H}, V_{\rm exp})$, and $k_3(N_{\rm H}, V_{\rm exp})$ for each geometry are shown in Table 1.

Fig. 2 compares the $f_{\rm esc}^{\rm Ly\alpha}$ computed analytically with equation (4) and with the free parameters obtained with the MCMC (lines), and that obtained with the full MC RT code (symbols) for a given values of $N_{\rm H}$ and $V_{\rm exp}$ and the three different geometries. The analytical expression reproduces remarkably well the results of the full MC RT code.

The accuracy of our analytic expressions varies with $\tau_{\rm a}$, $V_{\rm exp}$, $N_{\rm H,}$ and the geometry. In particular, there is a strong dependence on $\tau_{\rm a}$: for every geometry we find that the accuracy decreases with increasing $\tau_{\rm a}$. We find that, in general, the discrepancy with the full MC RT code in configurations with $\tau_{\rm a} > 10^{-0.5}$ becomes greater than 10 per cent. Galaxies with such a large dust absorption, in general, will not be observed as an LAE so we are not concerned about the low accuracy at high $\tau_{\rm a}$. Additionally, we checked that, after calibration of our LAEs model (see Section 3.1), less than 2 per cent of the Lyα selected galaxies (LAEs) in each geometry have $\tau_{\rm a} > 10^{-0.5}$, making the contribution of these galaxies negligible. For galaxies with $10^{-1.5} < \tau_{\rm a} < 10^{-0.5}$, the discrepancy is just a few per cents for $N_{\rm H}$ between 10^{19} and $10^{22.5}$ cm^{-2} and $V_{\rm exp}$ between

[2] http://dfm.io/emcee/current/

Table 1. Constant parameter values used to derive the escape fraction of the different geometries.

Thin shell	
$k_1 = k_{11} V_{\rm exp}^{k_{12}}$	$k_2 = k_{21} V_{\rm exp}^{k_{22}}$
$k_{11} = k_{111}(\log N_{\rm H_{18}})^2 + k_{112} \log N_{\rm H_{18}} + k_{113}$	$k_{21} = 10^{-0.0368}$
$k_{12} = k_{121}(\log N_{\rm H_{18}})^3 + k_{122}(\log N_{\rm H_{18}})^2 + k_{123} \log N_{\rm H_{18}} + k_{124}$	$k_{22} = 10^{-1.556}$
$k_{111} = 10^{2.109}$	
$k_{112} = -10^{2.745}$	
$k_{113} = 10^{2.954}$	
$k_{121} = 10^{-1.785}$	
$k_{122} = -10^{-0.730}$	
$k_{123} = 10^{-0.155}$	
$k_{124} = -10^{0.151}$	
Galactic wind	
$k_1 = k_{11} V_{\rm exp}^{k_{12}}$	$k_2 = k_{21} V_{\rm exp}^{k_{22}}$
$k_{11} = k_{111} N_{\rm H_{18}}^{k_{112}}$	$k_{21} = 10^{0.0137}$
$k_{12} = k_{121}(\log N_{\rm H_{18}})^2 + k_{122} \log N_{\rm H_{18}}$	$k_{22} = 10^{-1.62}$
$k_{111} = 10^{0.471}$	
$k_{112} = 10^{-0.244}$	
$k_{121} = 10^{-1.82}$	
$k_{122} = -10^{-0.667}$	
Biconical wind	
$k_1 = k_{11} V_{\rm exp}^{k_{12}} + k_{13}$	$k_2 = k_{21} V_{\rm exp}^{k_{22}}$
$k_{11} = 10^{3.229}$	$k_{21} = 10^{0.0470}$
$k_{12} = -10^{-0.0752}$	$k_{22} = 10^{-1.490}$
$k_{13} = k_{131}\ N_{\rm H_{18}}^{k_{132}} + k_{133}$	
$k_{131} = 10^{-0.580}$	
$k_{132} = 10^{-0.238}$	
$k_{133} = 10^{0.700}$	
$k_3 = k_{31} V_{\rm exp}^{k_{32}} + k_{33}$	
$k_{31} = 10^{k_{311}(\log N_{\rm H_{18}})^2 + k_{312}}$	
$k_{32} = k_{321}(\log N_{\rm H_{18}})^2 + k_{322} \log N_{\rm H_{18}} + k_{323}$	
$k_{33} = 10^{-0.0779}$	
$k_{311} = 10^{-0.874}$	$k_{321} = -10^{-1.226}$
$k_{312} = 10^{0.571}$	$k_{322} = 10^{-0.477}$
	$k_{323} = -10^{0.292}$

80 and 1000 km s^{-1}. Moreover, for $\tau_{\rm a} < 10^{-1.5}$ the discrepancy is typically below 1 per cent in the same parameter range. Appendix B shows the performance of our analytic expressions and the $\tau_{\rm a}$, $V_{\rm exp,}$ and $N_{\rm H}$ distributions of the LAE samples.

2.3 Simulation and semi-analytical model

We combine the radiative transfer code described above with the semi-analytical model of galaxy formation `galform` (Lacey et al. 2016) run on the `P-Millennium` *N*-body simulation (Baugh et al. 2019).

The `P-Millennium` is a state-of-the-art dark matter-only *N*-body simulation using the Planck cosmology: $H_0 = 67.77$ km s^{-1} Mpc^{-1}, $\Omega_\Lambda = 0.693$, $\Omega_{\rm M} = 0.307$, $\sigma_8 = 0.8288$ (Planck Collaboration XIII 2016). The box size is 542.16 cMpc h^{-1} and the particle mass $\rm M_p = 1.061 \times 10^8\ M_\odot\ h^{-1}$ (5040^3 dark matter particles). Between the initial redshift, $z = 127$, and the present, $z = 0$, there are 272 snapshots. In this work we use snapshots 77, 84, 120, and 136 corresponding to redshifts 6.7, 5.7, 3.0, and 2.2, respectively.

A full review on semi-analytical models of galaxy formation can be found in Baugh (2006). The variant of `galform` used in this work is based on earlier versions described in Cole et al. (2000), Baugh et al. (2005), and Bower et al. (2006). In brief, `galform` computes the properties of the galaxy population following the hierarchical growth of dark matter haloes. Halo merger trees are extracted from an *N*-body simulation (the `P-Millennium` in our case), so the model can also predict the spatial distribution and peculiar velocities of galaxies.

In `galform`, galaxies are formed and evolve as a result of the following processes: (i) the radiative cooling and the shock-heating of gas inside haloes; (ii) the subsequent cooling of gas forming a disc at the bottom of the potential well; (iii) quiescent star formation in the disc and starbursts in bulges resulting from disc instabilities and galaxy mergers; (iv) feedback processes (supernovae, active galactic nucleus, and photoionization) regulating the star formation, and (v) the chemical enrichment of stars and gas that results from star formation and feedback episodes. Additionally, the variant of `galform` used in this work assumes different initial mass functions (IMFs). In particular, a Kennicutt (1983) IMF is used for quiescent star formation, while for starburst modes a top-heavy IMF is implemented (see Lacey et al. 2016, for more details) .

`galform` generates a composite spectral energy distribution (SED) for each individual galaxy based on its star-forming history and computes the rate of emission of hydrogen ionizing photons, $\dot{Q}_{\rm H}$, by integrating the galaxy SED over wavelengths bluer than the Lyman break at $\lambda = 912$ Å. All ionizing photons are assumed to

be absorbed by the neutral medium. Then case B recombination (Osterbrock 1989) is used to compute the intrinsic line luminosity of Lyα, where a fraction of 0.66 of ionizing photons contribute to generating Lyα photons.

In this work we only make use of `galform` galaxies with $M_{\rm stellar} > 10^7 [\,{\rm M}_\odot\, h^{-1}]$. This stellar mass threshold translates in dark matter haloes with mass $M_{\rm h} > 10^{10} [\,{\rm M}_\odot\, h^{-1}]$, well above the halo mass resolution limit of the simulation, $\sim 2\ 10^9 [\,{\rm M}_\odot\, h^{-1}]$.

2.3.1 *Radiative transfer parameters*

To combine the Monte Carlo radiative transfer code with `galform`, we need to derive the parameters that define the neutral gas configuration from the galaxy output properties. In particular, the column density $N_{\rm H}$, expansion velocity $V_{\rm exp}$, and the optical depth of dust $\tau_{\rm a}$ are key to determine the escape fraction. Motivated by observational works (e.g. Cazzoli et al. 2016), the expansion velocity is computed for the three geometries as:

$$V_{\rm exp,c} = \kappa_{\rm V,c} {\rm SFR_c} \frac{r_{\rm c}}{M_*}, \tag{7}$$

where the index c denotes the galaxy component (disc or bulge), $\rm SFR_c$ and $r_{\rm c}$ are the SFR$[{\rm M}_\odot\,{\rm Gyr}\,h^{-1}]$ and half mass radius [pMpc] of each galaxy component, $M_*[{\rm M}_\odot\, h^{-1}]$ is the total stellar mass of the galaxy and $\kappa_{\rm V,c}$ are two (one per galaxy component) free parameters. Note that, in our model, the photons generated in each galaxy component do not interact with the outflow corresponding to the other galaxy component.

The neutral hydrogen column density is computed in different ways depending on the geometry (see Section 2.1) :

$$\rm N_{H,c} = \begin{cases} \kappa_{\rm N,c} \frac{M_{\rm cold,c}}{r_{\rm c}^2} & \text{Thin Shell} \\ \kappa_{\rm N,c} \frac{M_{\rm cold,c}}{r_{\rm c} V_{\rm exp,c}} & \text{Wind and Bicone} \end{cases} \tag{8}$$

where $M_{\rm cold,c}$ and $\kappa_{\rm N,c}$ are, respectively, the cold gas mass and a free parameter of the galaxy component c.

All the free parameters linking `galform` properties to $V_{\rm exp}$ and $N_{\rm H}$ are calibrated by fitting the observed LAE luminosity function at different redshifts. For further details, see Section 3.1.

Finally, $\tau_{\rm a}$ is computed for every geometry as:

$$\tau_{\rm a,c} = (1 - A_{\rm Ly\alpha}) \frac{E_\odot}{Z_\odot} N_{\rm H,c} Z_c, \tag{9}$$

where $A_{\rm Ly\alpha} = 0.39$ is the albedo at the Lyα wavelength, $E_\odot = 1.77 \times 10^{-21}$ cm^{-2} is the ratio $\tau_{\rm a}/N_{\rm H}$ for solar metallicity, $Z_\odot = 0.02$ (Granato et al. 2000), and Z_c is the cold gas metallicity of the galaxy component c.

The intrinsic Lyα LF predicted by `galform` (see Fig. 3) results from two populations: normal star-forming galaxies (populating the low-luminosity range) and galaxies with an ongoing star formation burst (populating the high-luminosity range). Consequently, the values of $\kappa_{\rm N,disc}$ and $\kappa_{\rm V,disc}$ control the shape of the faint-end LF, whereas $\kappa_{\rm N,bulge}$ and $\kappa_{\rm V,bulge}$ control the bright end of the LF. In both regimes, increasing (decreasing) $\kappa_{\rm N,c}$ leads to an increase (decrease) of the $N_{\rm H}$ distribution. This leads to a decreasing (increasing) in the resulting $f_{\rm esc}^{\rm Ly\alpha}$ distribution and thus lowers (increases) the number of galaxies with higher luminosities. Also, increasing (decreasing) $\kappa_{\rm V,c}$ leads to an increase (decrease) of the $V_{\rm exp}$ distribution, increasing (decreasing) $f_{\rm esc}^{\rm Ly\alpha}$ and the number of galaxies with high luminosities.

3 IMPLEMENTING LYα RADIATIVE TRANSFER IN A SEMI-ANALYTICAL MODEL

In this section we describe how we incorporate the Lyα radiative transfer processes inside the semi-analytical galaxies from `galform`. We make use of the fitting formula described above to predict the Lyα escape fraction and line profiles. The strategy to fit the value of the free parameters of equations (7) and (8) is described below.

3.1 Calibrating the model

In order to calibrate the model and compute the values of the free parameters for each geometry, we fit our model to the observed LAE luminosity function at redshifts $z = 2.2$, 3, 5.7, and 6.7. We run `emcee` (Foreman-Mackey et al. 2013b) to perform an MCMC to find the values of $\kappa_{\rm N,c}$, $\kappa_{\rm V,c}$. The dynamical range of each free parameter is determined by limiting the expansion velocity and column densities of each component to lie within $80 < V_{\rm exp}[{\rm km\ s^{-1}}] < 1000$ and $19.0 < \log(N_{\rm H}[{\rm cm^{-2}}]) < 22.5$ for at least 90 per cent of the resulting galaxy population with Lyα rest frame equivalent width ${\rm EW_0} > 20$ Å and Lyα luminosity $L_{\rm Ly\alpha} > 10^{41.5}$ erg s^{-1}. These limits are imposed by the range of validity of the fitting formulae to derive the escape fraction (see Section 2.2).

This calibration is done independently for each outflow geometry and individual redshift bin. To combine multiple observed LFs at redshifts 2.2 and 3.0 we compute a 5th-order polynomial fit (in logarithm of Lyα luminosity – logarithm LF space) taking into account the uncertainties of each survey to obtain a single curve that represents the observational measurements. We choose to use a 5th-order polynomial at these redshifts as some recent works suggest that the typical Schechter function is not able to reproduce the observe LF (Konno et al. 2016; Sobral et al. 2017). Additionally, at redshift 5.7 and 6.7 we use the best-fitting Schechter function to the observed LAE LF computed by Konno et al. (2018). The LF used to calibrate our model are shown in Fig. 3 in black dashed lines.

The model Lyα luminosity of galaxies, for each geometry and choice of $[\kappa_{\rm V,disc}, \kappa_{\rm V,bulge}, \kappa_{\rm N,disc}, \kappa_{\rm N,bulge}]$, is computed as follows: (i) we compute the intrinsic Lyα luminosity of each component, $L^0_{\rm Ly\alpha}$, of each galaxy, which is directly proportional to the ionizing photon production $\dot{Q}_{\rm H}$ predicted by `galform`; (ii) we compute $V_{\rm exp,disc}$, $N_{\rm H_I,disc}$ and $\tau_{\rm a,disc}$ using equations (8) and (9); (iii) we obtain $f_{\rm esc}^{\rm Ly\alpha}$ for each galaxy component using equation (4); (iv) the observed Lyα luminosity of each component is obtained by multiplying the intrinsic luminosities by their respective $f_{\rm esc}^{\rm Ly\alpha}$; and (v) the total Ly$\alpha$ luminosity for each galaxy is the sum of the observed luminosity of each component (disc+bulge).

Fig. 3 shows the observed LAE LF (points), the full `galform` intrinsic Lyα LF (thin black line), and the predictions for each geometry (thick colored lines), using the free parameters that result from the MCMC (listed in Table 2) at the different redshifts implemented in this work.

The intrinsic Lyα LF in divided into two populations: normal SFR galaxies in the low-luminosity range and starburst galaxies in the high-luminosity range. In general, in `galform` the galaxy disc component in dominated by a quiescent SFR while in bulges the main mode of star formation is starburst, although quiescent star formation is also included. Additionally, in `galform` the quiescent SFR and the starburst have different IMFs, which produces the bumps in the LF. On one hand, at lower redshifts, the predicted intrinsic LF is above the observations at all luminosities, thus galaxies at these redshifts require a significant $f_{\rm esc}^{\rm Ly\alpha} < 1$ in order

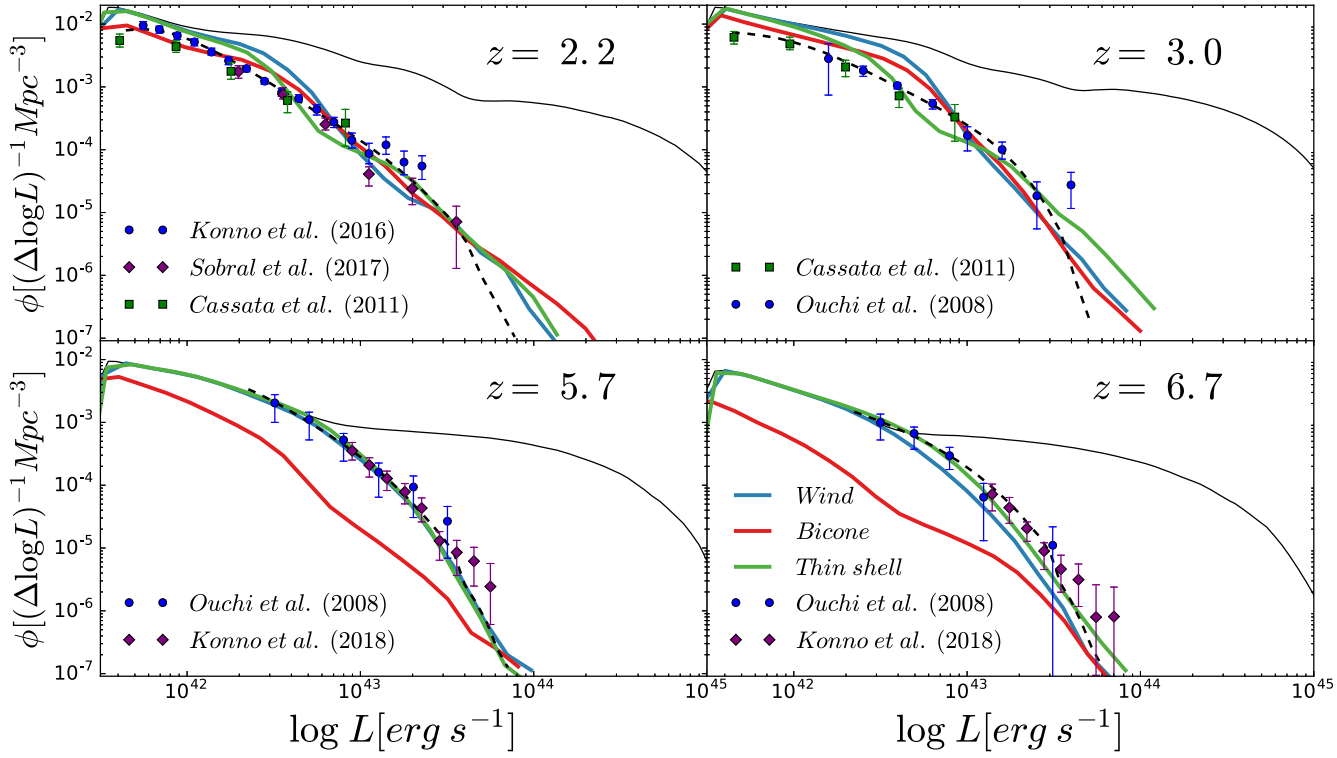

Figure 3. LAE LF at redshifts 2.2 (top left), 3.0, (top right), 5.7 (bottom left), and 6.7 (bottom right). The LF computed for different geometries is plotted as colored continuum lines, in blue for the *Wind* geometry, in red for the *Bicone* geometry and in green the *Thin Shell* geometry. In continuum black we show the intrinsic Lyα LF. The black dashed lines show the combined LF that is fitted that, at the same time, is the AM-noRT LF (detailed in Section 4) LF. At redshift 2.2 we also show the LF observed by Konno et al. 2016 (blue dots), Sobral et al. 2016 (purple diamonds), and Cassata et al 2011 (green squares). At redshift 3.0 we show the LF observed by Cassata et al 2015 (green squares) and Ouchi et al. 2008 (blue dots). At redshifts 5.7 and 6.7, we show the LF observed by Ouchi et al. 2008 (blue dots) and Konno et al. 2018 (purple diamonds).

Table 2. Free parameters as defined in equations (7) and (8) after the calibration with the observed luminosity function for different geometries and redshifts.

Redshifts	Geometry	$\log \kappa_{\rm V,disc}$	$\log \kappa_{\rm V,bulge}$	$\log \kappa_{\rm N,disc}$	$\log \kappa_{\rm N,bulge}$
$z = 2.2$	Thin Shell	4.440	4.911	− 12.367	− 11.839
	Wind	4.857	4.914	− 7.065	− 5.338
	Bicone	4.982	4.258	− 8.140	− 7.249
$z = 3.0$	Thin Shell	4.337	4.549	− 12.465	− 11.915
	Wind	4.691	4.769	− 7.440	− 5.166
	Bicone	4.896	4.338	− 8.436	− 6.404
$z = 5.7$	Thin Shell	4.737	4.428	− 13.906	− 11.808
	Wind	4.660	3.782	− 8.292	− 6.180
	Bicone	4.612	3.590	− 8.078	− 7.614
$z = 6.7$	Thin Shell	4.659	4.279	− 13.81	− 11.934
	Wind	4.589	3.871	− 8.073	− 5.910
	Bicone	4.455	3.561	− 7.848	− 7.647

to reduce the amplitude of the LF. On the other hand, at redshifts 5.7 and 6.7, the intrinsic LF at low $L_{\rm Ly\alpha}$ (disc-dominated region) matches observations, implying that galaxies in this range must have $f_{\rm esc}^{\rm Ly\alpha} \sim 1$. Additionally, the intrinsic high redshift LF at high luminosities (bulge-dominated regime) requires $f_{\rm esc}^{\rm Ly\alpha} < 1$.

In general, the MCMC approach finds good matching solutions for the models including the Lyα radiative transfer. First, we find that the *Thin Shell* is consistent with the measured LF at at all redshifts. Secondly, the *Wind* geometry performs quite well at $z = 2.2$, 3.0, and 5.7, while at $z = 6.7$ it underpredicts the number density of LAE. However, we have checked that by allowing $V_{\rm exp}$ to be slightly higher, the observed LF is matched at redshift 6.7 as well. In the third place, the *Bicone* geometry matches the observed LF at $z = 2.2$ and 3.0 while at $z = 5.7$ and 6.7 it fails. The low abundance of LAEs predicted with the *Bicone* geometry arises due to the low escape fractions predicted by this geometry. In fact, at high redshifts,

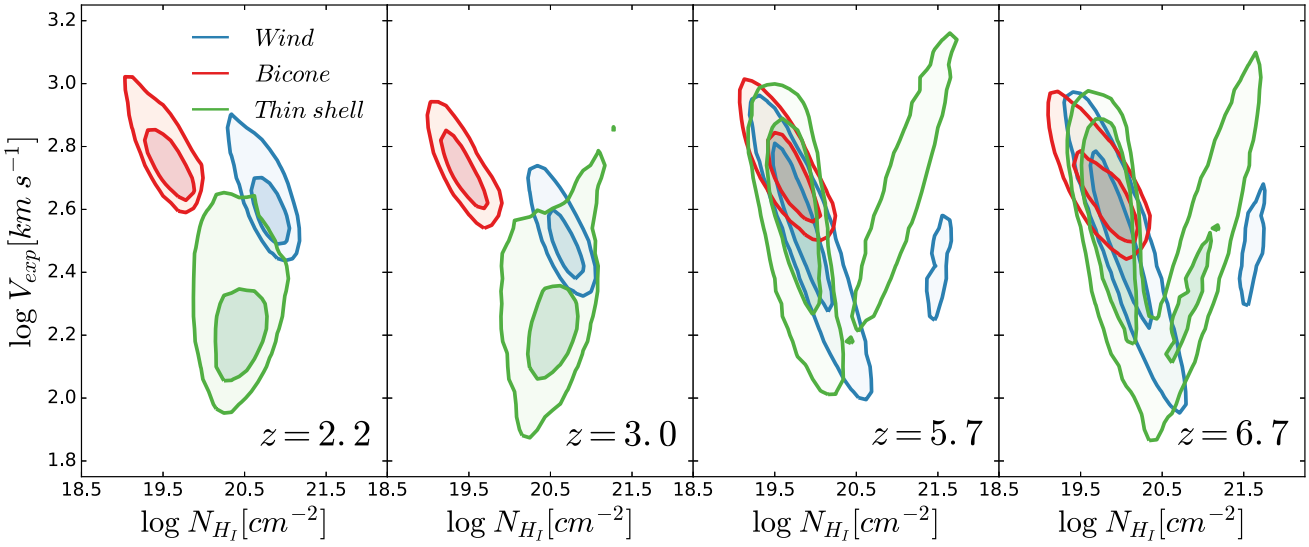

Figure 4. Ouflow expansion velocity and neutral hydrogen column density distributions for each redshift (z = 2.2, 3.0, 5.7, and 6.7 from left to right) and for each geometry colour coded as stated in the legend. The dark- and light-shaded contours enclose the 40 and 80 percentiles of the galaxy population, respectively.

faint Lyα emitters require escape fractions close to 1 to match the observed LFs, and this is not possible in the *Bicone* geometry by construction, as shown in Fig. 2.

3.2 A simplified model with no Lyα radiative transfer

In order to highlight how radiative transfer changes the properties of LAEs, we compare the properties of our model with an abundance matching approach. We perform a simple SFR-Lyα mapping where no Lyα radiative transfer is taken into account. We refer to this model variant as 'AM-noRT'.

To construct the AM-noRT model, we rank galaxies by their SFR. We assign a Lyα luminosity to each galaxy based on their total SFR in a monotonic way. Objects with the highest SFR are assigned the brightest Lyα luminosity. We compute the Lyα equivalent width using the assigned Lyα luminosity and continuum luminosity around the Lyα frequency provided by `galform`. Lyα luminosities are assigned recursively towards lower luminosities such that the Lyα observed luminosity function (using the EW_0 cut of each survey) is recovered at each redshift. The resulting Lyα luminosity distribution is shown in Fig. 3 as dashed black line. We compute a $f_{\rm esc}^{\rm Ly\alpha}$, which corresponds to the ratio between the assigned *Lyα* luminosity and the intrinsic one.

In contrast with our RT models, the $f_{\rm esc}^{\rm Ly\alpha}$ in the SFR-only model does not depend on properties such as the cold gas mass or the galaxy metallicity. Due to the way that Lyα luminosities are computed, the resulting $f_{\rm esc}^{\rm Ly\alpha}$ can be higher than 1 in some cases.

4 RESULTS

In this section we describe the main predictions of our radiative transfer model when applied to `galform` with the different outflow geometries.

4.1 The $N_{\rm H}$ and $V_{\rm exp}$ distributions

Since the parameters in our model are calibrated to match the observed LFs for each geometry independently, the resulting distributions of $N_{\rm H}$ and $V_{\rm exp}$ are different for each configuration. Through this work unless it is different stated, we define LAE as a galaxy with a Lyα rest frame equivalent width EW$_0$ > 20 Å as typically in the literature (e.g. Ouchi et al. 2018). In this section, we rank LAEs by their luminosity and select the brightest to achieve a number density of $10^{-3}\,h^3$ cMpc^{-3}.

Fig. 4 shows the distribution of $V_{\rm exp}$ and $N_{\rm H}$ for each geometry. Since each quantity is computed for the disc and bulge component of each galaxy separately, we weight each component by their observed Lyα luminosity to build the distributions shown in Fig. 4.

Overall, the $V_{\rm exp}$ − $N_{\rm H}$ distribution is relatively compact at redshifts (z = 2.2, 3.0) and more extended at higher redshift (z = 5.7, 6.7). The *Thin Shell* tends to have lower $V_{\rm exp}$ and $N_{\rm H}$ than the *Wind* geometry. Additionally, there is a strong difference between low and high redshifts for these two distributions, while, in the case of the *Bicone*, remains generally unchanged across cosmic time. Additionally, most of the galaxies lie within the $f_{\rm esc}^{\rm Ly\alpha}$ analytic expression optimal accuracy region defined in Section 3. Moreover, we have checked that the fraction of galaxies outside this region is lower than a 7 per cent for every geometry and redshift.

Typical values $V_{\rm exp}$ are found to be around 150 km s^{-1} and 300 km s^{-1} for the *Thin Shell* and *Wind* geometries, respectively, at z = 2.2, 3.0. Meanwhile, $N_{\rm H}$ is found at $\sim 10^{20.5}$ cm^{-2} for the *Thin Shell* and $\sim 10^{20.8}$ cm^{-2} for the *Wind*. Notably, at higher redshifts, z = 5.7 and 6.7, the distributions acquire a 'V' shape (especially visible for the *Thin Shell*) due to the division of each `galform` galaxy into a disc and bulge and the significant difference in $f_{\rm esc}^{\rm Ly\alpha}$ for starburst and normal SFR galaxies at these redshifts. Lower column densities are favored by disc-dominated galaxies, requiring a higher $f_{\rm esc}^{\rm Ly\alpha}$ in order to fit the LF. the distribution of these galaxies peak around $N_{\rm H} \sim 10^{19.7}$ cm^{-2} and $V_{\rm exp} \sim 300$ km s^{-1}. Bulge-dominates starbursts require a lower $f_{\rm esc}^{\rm Ly\alpha}$ to fit the LF, thus they favour high $N_{\rm H}$ and low $V_{\rm exp}$ distributions centred around $10^{21.0}$ cm^{-2} and 200 km s^{-1}, respectively.

The *Bicone* geometry displays noticeable differences with respect to the other two geometries. The *Bicone* $V_{\rm exp}$ − $N_{\rm H}$ distributions are very similar across the different redshifts used in this work and present the available highest $V_{\rm exp}$ and lowest $N_{\rm H}$ distributions (peak-

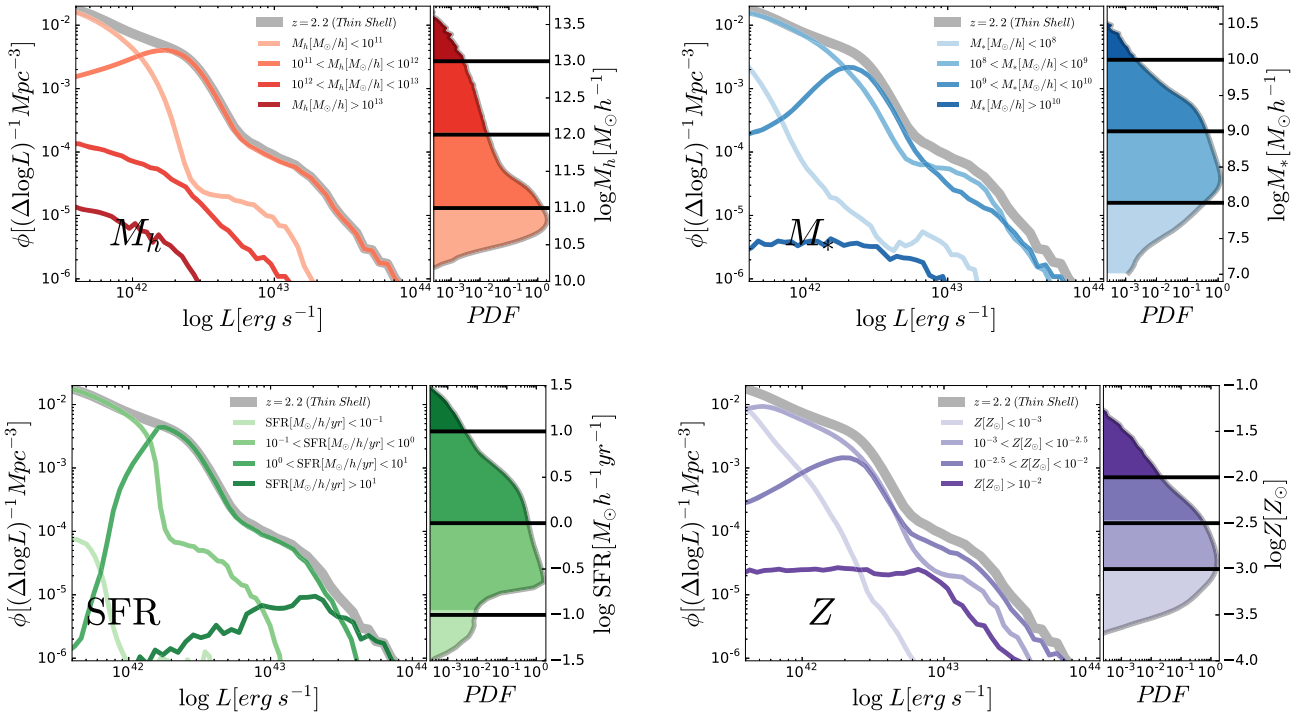

Figure 5. *Left-hand panels* : Breakdown of the Lyα LF at $z = 2.2$ of galaxies with Lyα EW$_0$ > 20 Å in bins of halo mass (upper left), stellar mass (upper right), star formation rate (lower left), and metallicity (lower right). The bins are indicated in the legends. In each quantity the bins are represented in lighter colors for low values and darker as they increase. The total LF is plotted in thick grey line. *Right-hand panels*: The probability distribution function of the different properties. In black we show the bin cuts.

ing around 600 km s^{-1} and $10^{19.2}$ cm^{-2}, respectively), maximizing as much as possible the escape of Lyα photons. This is due to the fact that the typical $f_{\rm esc}^{\rm Ly\alpha}$ is always lower in the *Bicone* compared to the other geometries, and it never reaches 1.

On one hand, at low redshift ($z = 2.2$, 3.0) our models fit the observed Lyα LF. At these redshifts, the *Bicone* is able to predict low enough $N_{\rm H}$ and high enough $V_{\rm exp}$ to reproduce the observed LAE number counts. The $N_{\rm H}$ and $V_{\rm exp}$ values in the *Bicone* are lower and higher, respectively, than in the other geometries, thus enhancing $f_{\rm esc}^{\rm Ly\alpha}$.

On the other hand, at high redshift ($z = 5.7$, 6.7) the *Bicone* is not able to select lower (higher) $N_{\rm H}$ ($V_{\rm exp}$) as these values fall outside of the parameter grid (see Section 2.2). Thus, the Lyα LF with this geometry is not able to fit the observed LF, as shown above.

4.2 Breaking down the Lyα LF

To illustrate the properties of LAEs, Fig. 5 shows the Lyα LF obtained with the *Thin Shell* geometry at $z = 3.0$, split by the contribution of different ranges of halo and stellar mass, star formation rate, and gas metallicity. We note that other redshifts and geometries show a similar behaviour to what is shown in Fig. 5. Here we are analyzing a subsample composed of every LAE (EW$_0$ > 20 Å) with Lyα luminosity >$10^{41.5}$ erg s^{-1}.

When splitting the LF based on the halo mass of LAEs (upper-left panel), we find that the majority of LAEs are hosted by haloes of moderate mass, $M_{\rm halo} \sim 10^{11-12}[{\rm M}_\odot\, h^{-1}]$, which dominates the bright and moderate luminosities. LAEs with host halo masses below $M_{\rm halo} \lesssim 10^{11}[{\rm M}_\odot\, h^{-1}]$ dominate the very faint end of the LF, with $L_{\rm Ly\alpha} \approx 10^{41}$[erg s^{-1}]. Finally, the most massive haloes host galaxies do not contribute significantly to the LF shape. Furthermore, we have checked that there is no clear correlation between halo mass and Lyα luminosity.

In the upper right panel in Fig. 5 the LF is split according to the stellar mass of the emitting galaxy. The whole body of the LF is dominated by LAEs with stellar mass about $M_{\rm stellar} \sim 10^{8-10}[{\rm M}_\odot\, h^{-1}]$. Moreover, galaxies with a very low ($M_{\rm stellar} < 10^{8}[{\rm M}_\odot\, h^{-1}]$) or a very high ($M_{\rm stellar} > 10^{9}[{\rm M}_\odot\, h^{-1}]$) stellar mass do not contribute to bright or the faint ends. As in the $M_{\rm h}$ case, we do not find any clear correlation between stellar mass and Lyα luminosity.

The star formation rate, as expected, contributes in a roughly monotonic way to the Lyα LF. The faint-end of the Lyα LF is dominated by galaxies with low $\log(\mathrm{SFR}[{\rm M}_\odot\, h^{-1}\ {\rm yr}^{-1}]) \sim -0.5$. Additionally, the intermediate luminosities are dominated by moderate SFR $\sim 1 - 10[{\rm M}_\odot\, h^{-1}\ {\rm yr}^{-1}]$ while the bright end is populated by galaxies with the highest SFR (although with a significant scatter). Note that this trend only means that the $L_{\rm Ly\alpha}$ of LAEs scales with SFR, but not that every galaxy with high SFR would result in an LAE. Finally, we note that typically, galaxies with SFR $< 0.1[{\rm M}_\odot\, h^{-1}\ {\rm yr}^{-1}]$ do not contribute to the LF in our luminosity ranges, although they might dominate the very faint end of the Lyα LF.

The breakdown of the Lyα LF in terms of gas metallicity is less intuitive. Naively one would expect to find an anticorrelation between metallicity and Lyα luminosity, since $f_{\rm esc}^{\rm Ly\alpha}$ decreases with increasing dust, and thus, metallicity. However, we find the opposite: for LAEs with $\log(Z) < -2$, the low metallicity bins contribute to the lower luminosities and vice versa. This trend is broken for $\log(Z) > -2$ due to the low $f_{\rm esc}^{\rm Ly\alpha}$ at this metallicity range. The galaxies with highest Z do not contribute anymore to the bright end but to low and average luminosities. This leads to the bulk of the Lyα emitter population being dominated by galaxies with average

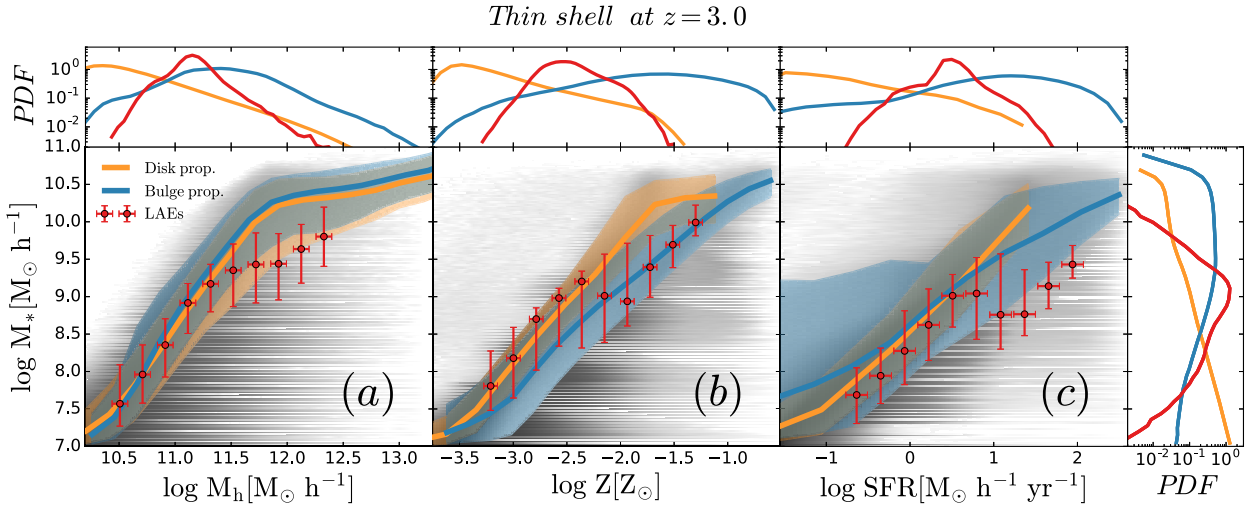

Figure 6. (a) The stellar mass – halo mass distribution at $z = 3.0$. The grey-shaded region shows the distribution for the full `galform` sample. The solid yellow and blue lines correspond to the median of `galform` central galaxies disc and bulges properties, respectively. The shade regions show the 10–90 percentiles. The red dots show the *Thin Shell* LAE sample median, 10–90 percentiles (vertical) and the bin size (horizontal). (b) Same as (a) but for the stellar mass – metallicity distribution. (c) Same as (a) but for the stellar mass – star formation distribution. The top panels show the distributions of the halo mass, star formation, and metallicity, respectively, for the full `galform` (yellow and blue for disc and bulge dominated, respectively) and the *Thin Shell* model (red). The stellar mass distribution is shown in the right vertical panel.

metallicities, spanning the range $-3 < \log(Z) < -2$. We dig deeper in this relation in Section 4.3

4.3 The bulk properties of LAEs

In this section we analyse the galaxy properties of our simulated LAE, focusing on the results at redshift $z = 2.2$ and for the *Thin Shell* geometry (we checked that different geometries and redshifts give similar results). We restrict our analysis only to the brightest central LAEs with a 10^{-3} cMpc$^{-3}h^3$ number density cut (we check that different number density cuts produce similar results), and we compare it with the properties of the underlying population of central galaxies, i.e. the full population of galaxies predicted by `galform` with $M_{\rm stellar} > 10^7[\,{\rm M}_\odot\,h^{-1}]$.

Fig. 6 shows some physical properties of the LAEs (red dots) and for the general population of galaxies from `galform` selected using the same number density cut as the LAEs (yellow for disc properties and blue for bulge properties). Each panel includes the distribution of halo mass $M_{\rm h}$, star formation rate SFR, metallicity Z, and stellar mass M_* and the correlation between $M_* - M_{\rm h}$, M_* – SFR and $M_* - Z$.

The $M_{\rm h}$ distribution in the LAE sample peaks at intermediate $M_{\rm h} \sim 10^{11}\,{\rm M}_\odot h^{-1}$ and spans between $10^{10.5}$–$10^{12}[\,{\rm M}_\odot h^{-1}]$. LAEs haloes trace the massive end of the disc-dominated $M_{\rm h}$ distribution while avoiding the most massive dark matter haloes, even if they host the strongest starburst episodes. This is caused by the SFR $- Z$ predicted by `galform` that associates high metallicites (low $f_{\rm esc}^{\rm Ly\alpha}$) with high SFR.

The metallicity and the SFR of the LAE sample behave in a similar way due to the tight SFR $- Z$ relation. The bulk of the LAE sample peaks at intermediate values of Z and SFR, avoiding the extremes of the full `galform` distribution. In particular, the galaxies with the highest SFR are not selected as LAE as the metallicity is also too high, causing a lower $f_{\rm esc}^{Ly\alpha}$. Additionally, the galaxies with extreme low Z are not selected either as their SFR in too low in these galaxies.

The $M_* - M_{\rm h}$ relations (Fig. 6) for disc- and bulge-dominated galaxies behaves in the same way. On the other hand, in the LAE sample this relation is the same as in the underlying galaxy population up to the peak of the $M_{\rm h}$ and M_* distributions, where the relation flattens for higher halo masses. In the high halo mass regime, LAEs typically have lower stellar masses than the overall average. This behaviour is given by the tight SFR $-$ Z relation causing $f_{\rm esc}^{Ly\alpha}$ to be lower for galaxies with higher M_* as they become more dust rich.

In the LAE sample, the SFR $- Z$ relation is consistent with the bulk of the disc-dominated galaxies for $Z < 10^{-2.5}{\rm Z}_\odot$. After a transition around $Z \sim 10^{-2.2}, {\rm Z}_\odot$ is consistent with starburst galaxies. At metallicities below that transition the LAE SFR $-$ Z relation is slightly above the overall relation.

In the LAE sample the M_* – SFR relation is below the full `galform` relation. This implies that for a fixed stellar mass, galaxies with higher SFR are selected, as the intrinsic $L_{\rm Ly\alpha}$ correlates directly with the SFR.

4.4 The predicted Lyα $f_{\rm esc}^{\rm Ly\alpha}$ against observational estimates

In this section we compare our model predictions for the $f_{\rm esc}^{\rm Ly\alpha}$ against observational estimates from Oyarzún et al. (2017) at $z = 3$. In order to mimic their sample selection function, we select galaxies with $10^{7.6}\,{\rm M}_\odot < M_* < 10^{10.6}\,{\rm M}_\odot$, and $L_{\rm Ly\alpha} > 10^{41.5}[{\rm erg\ s^{-1}}]$.

Fig. 7 shows the relation between the Lyα $f_{\rm esc}^{\rm Ly\alpha}$ and the SFR and stellar mass. The $f_{\rm esc}^{\rm Ly\alpha}$ computed in Oyarzún et al. (2017) displays a noticeable anticorrelation between SFR and $f_{\rm esc}^{\rm Ly\alpha}$. In the models including RT, galaxies with higher SFR have lower values of $f_{\rm esc}^{\rm Ly\alpha}$, in remarkable agreement with the observational estimates. The scatter in the observational data of Oyarzún et al. (2017) is consistent with the spread predicted by our models. This anticorrelation is caused by an intrinsic link between SFR and Z. Even if the $V_{\rm exp}$ is higher for greater SFR (equation 7), dust plays the major role in the escape of Lyα photons and reduces $f_{\rm esc}^{\rm Ly\alpha}$.

The stellar mass is also anticorrelated with the $f_{\rm esc}^{\rm Ly\alpha}$, as shown in the right-hand panel of Fig. 7. This is due to the known

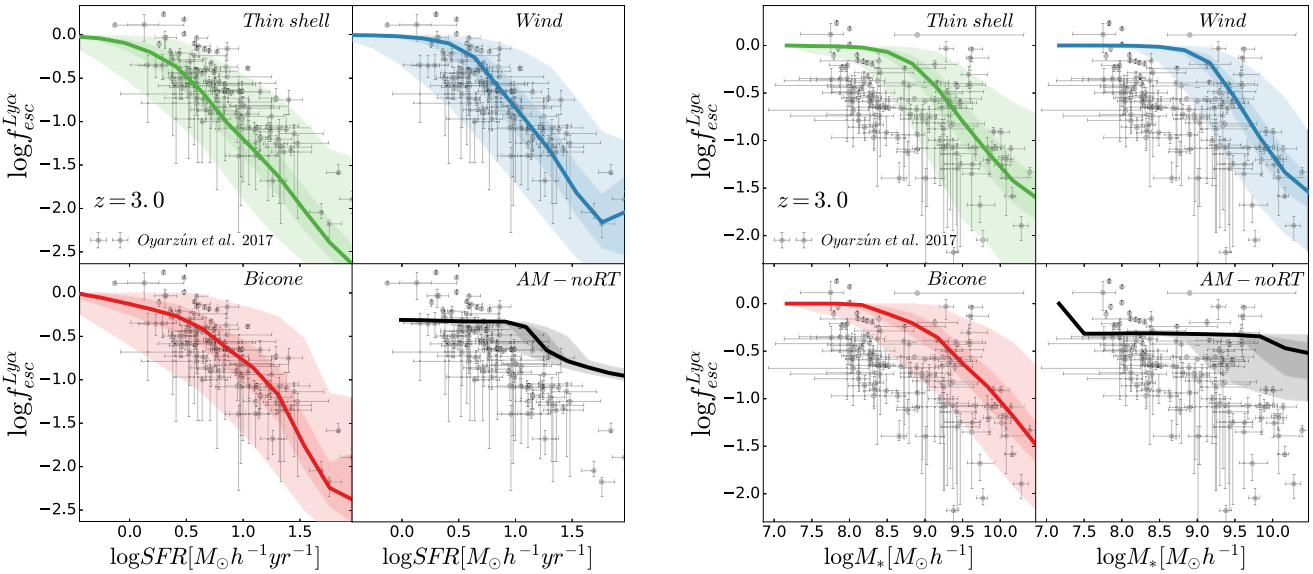

Figure 7. The Lyα $f_{\rm esc}^{\rm Ly\alpha}$ as a function of SFR (left-hand panels) and stellar mass (right-hand panels) at $z = 3$. Gray points are from Oyarzún et al. (2017). Each panel displays our model predictions with a different outflow geometry, as shown in the legend. The bottom-right corner displays the predictions of the model with no radiative transfer. The solid line in each panel is the median of $f_{\rm esc}^{\rm Ly\alpha}$ predicted by our models. The dark- and light-coloured shaded regions display the 32–68 and 5–95 percentiles of the models predictions, respectively.

correlation between M_* and Z. Although our models reproduce the observationally inferred trend, the stellar masses predicted by `galform` are systematically larger by ∼0.5 dex. In particular, Mitchell et al. (2013) compared stellar masses, using different stellar population models and `galform` stellar masses. They conclude that the uncertainty in the choice of stellar population model and parameters can lead to biased stellar masses by a factor of 0.5dex.

Interestingly, the abundance matching model AM-noRT does not display the same trends found in Oyarzún et al. (2017), highlighting the importance of considering radiative transfer effects to predict LAE galaxy properties consistent with observational data sets.

4.5 The dark matter haloes hosting LAEs

In the following we study the properties of dark matter haloes hosting LAEs. To compare different model predictions, we select the brightest LAEs with a number density cut of $10^{-3}\,h^3\,{\rm cMpc}^{-3}$.

Fig. 8 shows the halo occupation distribution (HOD) at $z = 2.2, 3.0, 5.7$, and 6.7. This is constructed by computing the mean number of galaxies within different halo mass bins. All models including radiative transfer display a similar HOD at $z = 2.2$ and 3.0. Central galaxies have a peak abundance in haloes of mass $M_{\rm halo} \approx 2 \times 10^{11}\,{\rm M}_\odot\,h^{-1}$. Satellite galaxies start dominating the abundance of haloes of mass $M_{\rm halo} \gtrsim 10^{12}\,{\rm M}_\odot\,h^{-1}$. None of the HODs at these redshifts reach $N(M_h) = 1$. Even at the peak of occupation, less than 10 per cent of haloes host an LAE, regardless of radiative transfer effects.

At $z \geq 5.7$ the HOD of the *Bicone* model falls significantly below that from the *Thin Shell* and *Wind* models. This reflects the differences in the LFs at these high redshifts. As the *Bicone* model is not able to reproduce the observed LF, the resulting LAE population has quite different properties to the other RT samples.

The model with no radiative transfer systematically places LAEs in higher mass haloes compared to the radiative transfer models at low redshift. The occupation peak for centrals in the AM-noRT model is shifted to slightly more massive haloes at $z = 2.2$ and 3.0. Additionally, at these redshifts, the occupation of dark matter haloes with $M_{\rm h} \geq 10^{12}\,{\rm M}_\odot\,h^{-1}$ is much greater in the AM-noRT model than in the models including RT. At redshifts $z = 5.7$ and 6.7, the trend is inverted as LAE (*Thin Shell* and *Wind* geometry) populate haloes slightly more massive than the AM-noRT model. Also, the occupation of haloes with $M_{\rm h} \geq 10^{12}\,{\rm M}_\odot\,h^{-1}$ is greater in the RT models.

The bottom panels of Fig. 8 show the quantity

$$b(M_h) N_{\rm LAE}(M_h) / N_{\rm galaxies}(M_h), \tag{10}$$

where $N_{\rm LAE}(M_h)$ is the number of sources in our LAEs samples in a halo mass bin, $N_{\rm galaxies}(M_h)$ is the number of galaxies in the same M_h bin and the galaxy bias $b(M_h)$ is defined as

$$\xi_{\rm galaxy} = b^2\,\xi_{\rm dark\ matter}, \tag{11}$$

where $\xi_{\rm galaxy}$ and $\xi_{\rm dark\ matter}$ are the two-point correlation functions for the galaxies and dark matter. This exhibits the contribution of different mass bins to the overall clustering bias of the LAE population. There is an evolution in the $M_{\rm h}$ that contributes to the bias, being greater at lower redshifts and lower at higher redshift. In particular, the peak values varies from $M_{\rm halo} \approx 2 \times 10^{11}\,{\rm M}_\odot\,h^{-1}$ at $z = 2.2$ to $\approx 6 \times 10^{10}\,{\rm M}_\odot\,h^{-1}$ at $z = 6.7$.

At low redshift ($z = 2.2$ and 3.0) the greater contribution to the bias come from lower mass haloes in the RT models than in the AM-noRT model. However, this trend is inverted at $z = 5.7$. Additionally, at $z = 6.7$ the main contribution to the bias comes from the same halo mass for all the models.

Overall there is a good agreement among some theoretical (e.g. Jose, Srianand & Subramanian 2013; Garel et al. 2015) and observational (e.g. Hagen et al. 2014; Kusakabe et al. 2018) work that predict/observed that LAE reside in dark matter haloes with masses about $10^{11}\,{\rm M}_\odot$ and present stellar masses around 10^8–$10^9\,{\rm M}_\odot$.

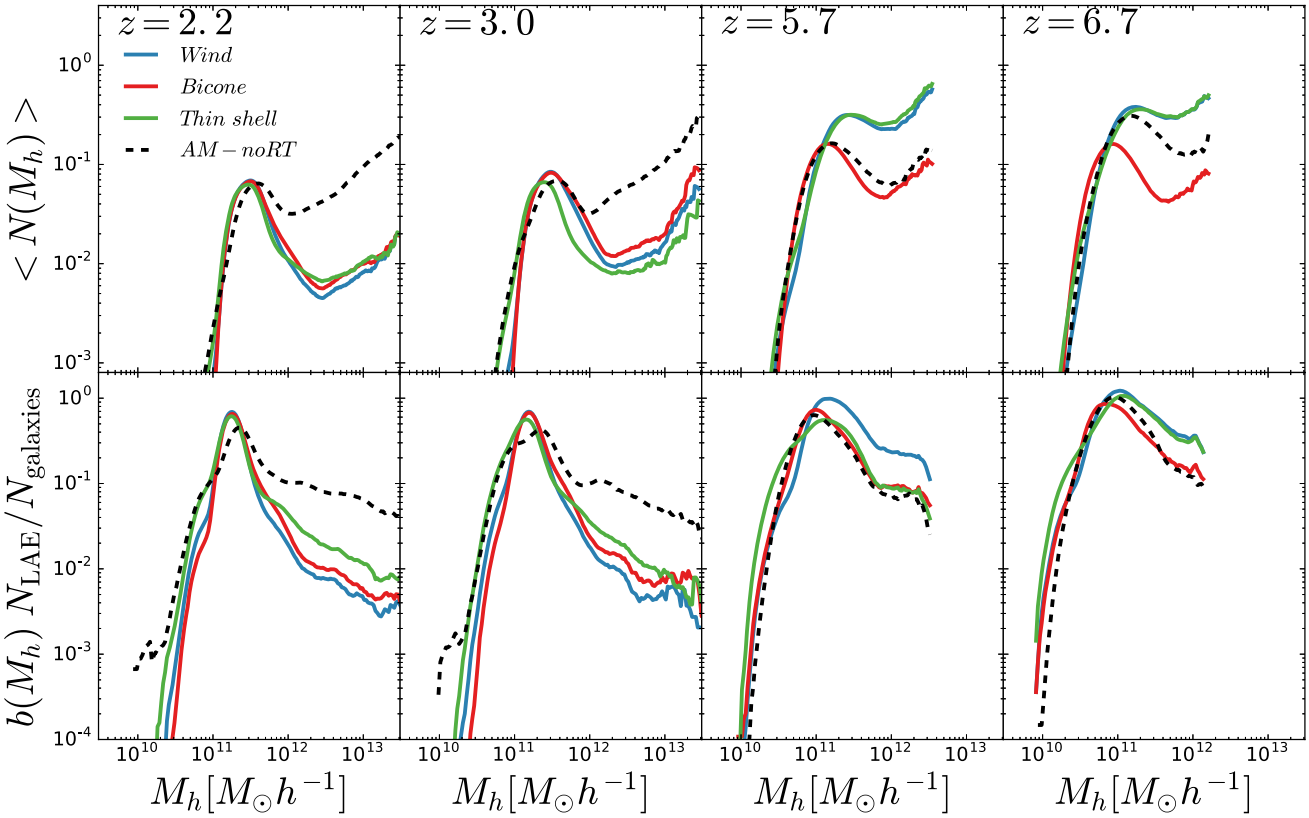

Figure 8. *Top*: the halo occupation distribution (HOD) at redshifts 2.2, 3.0, 5.7, and 6.7 from left to right. Model with radiative transfer show as blue, red, and green solid lines for the *Wind*, *Bicone,* and *Thin Shell* geometry, respectively. The LAE sample AM-noRT is plotted as dashed black line. *Bottom*: fraction of galaxies that are considered LAE times the bias of the hosting dark matter halo. This quantifies the contribution of the different $M_{\rm h}$ to the overall bias of the population.

4.6 The clustering of LAEs

In this section we study how Lyα radiative transfer impacts the clustering of LAEs for each of the outflow geometries implemented. The sample used in this section is the same as the one used in Section 4.5.

In Fig. 9 the top panel shows the spherically averaged 2-point auto-correlation function (2PCF) in real space at $z = 2.2$, 3.0, 5.7, and 6.7. The middle panel shows the bias, defined as in equation (10). Moreover, in order to highlight the differences in the RT samples and the AM-noRT, we show in the bottom panel of Fig. 9 the relative difference of the 2PCF of the LAE samples $\xi_{\rm LAE}$ and the AM-noRT, i.e. $\Delta\xi/\xi = (\xi_{\rm LAE} - \xi_{\rm AM\text{-}noRT})/\xi_{\rm AM\text{-}noRT}$, where $\xi_{\rm AM\text{-}noRT}$ is the AM-noRT 2PCF.

Overall, the clustering amplitude increases towards higher redshifts regardless of the LAE model variant. In detail, each model predicts a slightly different clustering bias. There is a strong scale dependence of the clustering bias in all models and at all redshifts for separations below $r \lesssim 15$–20 [Mpc h^{-1}].

At $z = 2.2$ and 3.0 the clustering amplitude of the AM-noRT sample is about 10 per cent above the one predicted by the RT models. This is a consequence of LAEs being hosted by higher mass dark matter haloes for this model, as shown in previous sections. At $z = 5.7$ and 6.7, the clustering amplitude of the *Thin Shell* and *Wind* LAE samples are above that of the AM-noRT and *Bicone* models. Interestingly, as shown in the bottom panels of Fig. 9, towards redshifts $z > 3$ the AM-noRT sample features a slightly different slope with respect to the RT models.

In summary, the predicted clustering of LAEs at $z \lesssim 3$ is overall slightly lower when radiative transfer is included, and slightly higher towards $z \gtrsim 3$. The relative differences in the amplitude of clustering, with respect to the AM-noRT model, are of the order of 10 per cent. These differences result from the non-trivial relation between the Lyα luminosity of galaxies and the dark matter halo population hosting these objects.

4.7 The clustering in mock catalogues of LAE surveys

In this section we compare our clustering prediction against several measurements of the clustering of LAEs at different redshifts from Kusakabe et al. (2018) at $z = 2.2$, Bielby et al. (2016) at $z = 3.0$, and Ouchi et al. (2010, 2018) at $z = 5.7$ and 6.7, respectively. We build LAE mock catalogues mimicking the properties of the different surveys to allow a close comparison with the observational data sets. These surveys use narrow-band photometry to detect LAEs over a restricted redshift range. The main difference in the mock catalogues comes from the specific area, flux depth, and equivalent width limit (EW) of the individual survey.

To build the mock catalogues, we choose a direction as LoS. Assuming a distant observer, a galaxy coordinate is transformed in redshift space using

$$s = x_{\rm LoS} + \frac{{\rm v}_{\rm LoS}}{a(z)H(z)}, \tag{12}$$

where $x_{\rm LoS}$ is the galaxy coordinate along the LoS, ${\rm v}_{\rm LoS}$ is the galaxy peculiar velocity along the LoS, and $a(z)$ and $H(z)$ are the

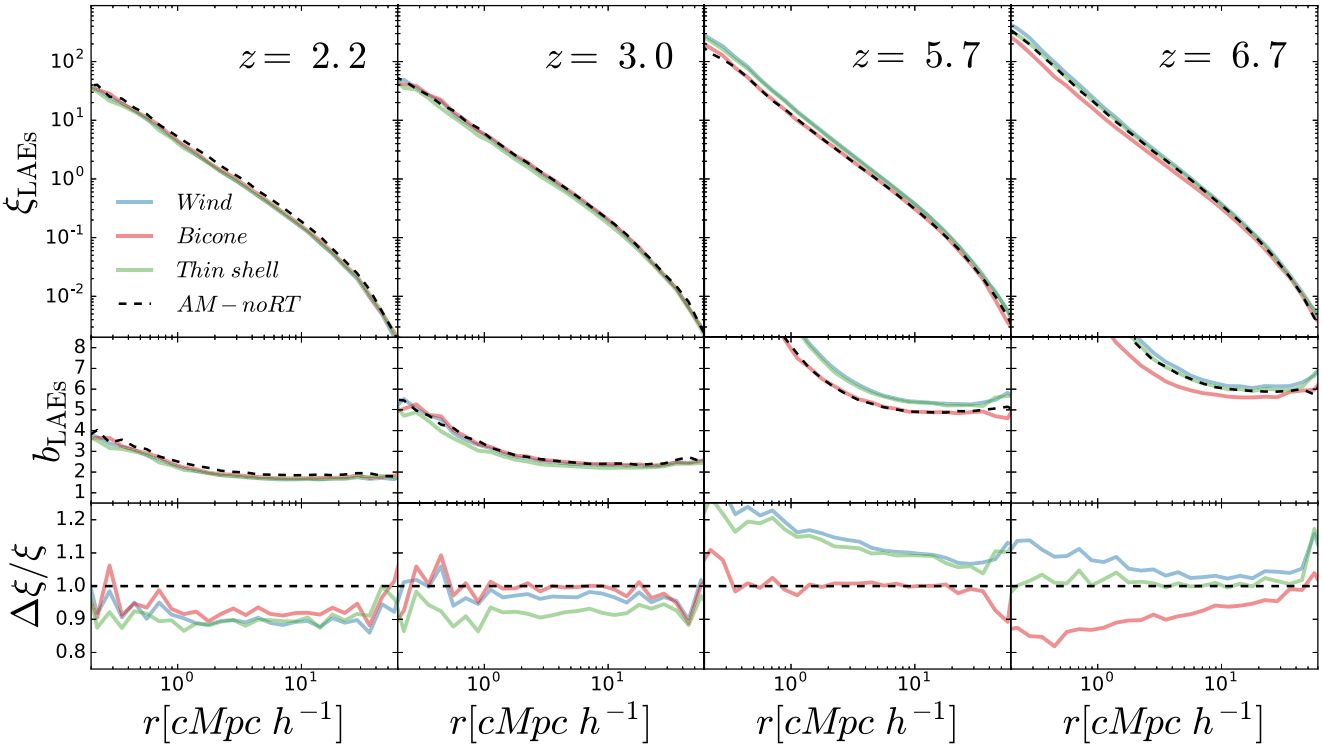

Figure 9. *Top panels* : 3D auto-correlation function for the AM-noRT sample (black), for the *Thin Shell* (green), galactic wind (blue), and biconical galactic wind (red) for redshifts 2.2, 3.0, 5.7, and 6.7 from left to right. *Middle panels* : The ratio between the different LAE sample and the dark matter correlation function. *Bottom panels*: relative difference between the different samples and the AM-noRT 3D correlation function.

scale factor and the Hubble parameter, respectively, at the Lyα pivot redshift, $z_{\rm pivot}$, of the NB filter. Additionally, we conserve the periodicity of the box along the LoS direction.

Although some surveys have complicated footprints due to multiple pointings, our mocks are constructed as squares comprising an area equal to that of the target survey. Thus, the simulation box is simply split in slices along the LoS. The size perpendicular to the LoS is computed as

$$L_\perp = \sqrt{A_{\rm survey}}, \tag{13}$$

where $A_{\rm survey}$ is the survey sky coverage. The thickness (along the LoS) of the slice is computed as

$$L_\parallel = D_{\rm co}(z = z_+) - D_{\rm co}(z = z_-), \tag{14}$$

where $D_{\rm co}(z)$ is the comoving distance at the geometric redshift z. Additionally,

$$z_\pm = \frac{\lambda_p \pm 0.5\ {\rm FWHM}}{\lambda_{{\rm Ly}\alpha}} - 1, \tag{15}$$

where λ_p and FWHM are the pivot wavelength and the full width half maximum of the narrow-band filter and $\lambda_{{\rm Ly}\alpha}$ is the Lyman α wavelength.

We calculate the limiting luminosity $L_{\rm cut}$ and the minimum rest frame equivalent width ${\rm EW}_{0,\rm cut}$ for each survey by matching the LAE number density, $n_{\rm LAE}$ of the surveys to the one in the whole simulation box (see Appendix C). Then, our mock catalogues consist of galaxies with luminosity above $L_{\rm cut}$ and ${\rm EW}_0$ above ${\rm EW}_{0,\rm cut}$. Table 3 lists the properties of the mocks, including the parallel and transverse sizes along the LoS, the redshift window $\Delta z = z_+ - z_-$, the number of mocks, $N_{\rm mock}$, sliced from the simulation box and the number of LAE in each survey, and the median with 32–68 percentiles of the number of LAEs in the mocks.

The value of $L_\parallel$ for narrow-band surveys is typically very small compared to the box length of the simulation. This allows for a big fragmentation of the simulation box along the LoS. On the other hand, $L_\perp$ can vary significantly between surveys. While, at low redshift ($z = 2.2$, 3.0) $L_\perp$ is relatively small and allows a large number of mock surveys, at $z = 5.7$, 6.7 only one cut is possible due to the large size required for the mock surveys. As a result of this, the number of mocks at $z = 2.2$, 3.0 (448 and 468, respectively) is much larger than that at $z = 5.7$, 6.7 (18 and 19, respectively).

Since $n_{\rm LAE}$ in the simulation box is set to match the observed $n_{\rm LAE}$ of each survey (see Appendix C), the observed number of LAE and the median number of LAE in our mocks, $\langle N_{\rm LAE}\rangle$, are compatible within 1σ. Additionally, the dispersion of $\langle N_{\rm LAE}\rangle$ is higher (lower) at $z = 2.2$ and 3.0 (5.7 and 6.7), since the comoving volume is smaller (larger). Hence, the impact of cosmic variance on clustering measurements is stronger (weaker).

We construct mock catalogues of LAE surveys from Kusakabe et al. (2018) at $z \approx 2.2$, Bielby et al. (2016) at $z \approx 3$, Ouchi et al. (2010) at $z \approx 5.7$ and Ouchi et al. (2018) at $z \approx 6.7$. Fig. 10 shows the comparison between the observed angular 2-point correlation function of these surveys, $\omega_{\rm survey}$, and that computed from the mock catalogues, $\omega_{\rm mock}$. Note that in Bielby et al. (2016) the authors rescaled their observed clustering by a factor of 1.64 to correct for contaminants. This kind of correction was not made in the other works used in this section. Here we use the Bielby et al. (2016) data set including their correction.

Overall, $\omega_{\rm mock}$ is very similar among our different model variations, including the AM-noRT model. The differences in the clustering due to the different bias of the samples are small in

Table 3. Mock catalogue characteristics including the redshift z, the redshift width Δz, sky coverage (Area), the size along the line of size $L_{\parallel}$, the distance perpendicular to the LoS $L_{\perp}$, the number of mocks sliced from the simulation box $N_{\rm mocks}$ and the median number of LAEs the mocks $\langle N_{\rm LAE}\rangle$ with the 32 and 68 percentiles.

Authors	z	Δz	Area (deg^2)	$L_{\parallel}$ (cMpc)	$L_{\perp}$ (cMpc)	$N_{\rm mocks}$	$\langle N_{\rm LAE}\rangle$ Survey	Thin shell	Wind	Bicone	AM-noRT
Kusakabe et al. (2018)	2.2	0.0773	0.93	104.9	93.6	448	1248	1196^{+94}_{-90}	1191^{+95}_{-80}	1189^{+105}_{-78}	1183^{+109}_{-91}
Bielby et al. (2016)	3.0	0.0633	1.07	60.0	119.1	468	643	639^{+48}_{-57}	639^{+53}_{-51}	637^{+52}_{-60}	631^{+66}_{-59}
Ouchi et al. (2018)	5.7	0.0954	7.67	43.5	401.5	18	734	725^{+15}_{-9}	731^{+11}_{-19}	720^{+19}_{-21}	719^{+16}_{-20}
Ouchi et al. (2018)	6.7	0.1078	21.2	41.0	696.5	19	873	873^{+6}_{-30}	865^{+17}_{-19}	864^{+21}_{-20}	866^{+24}_{-6}

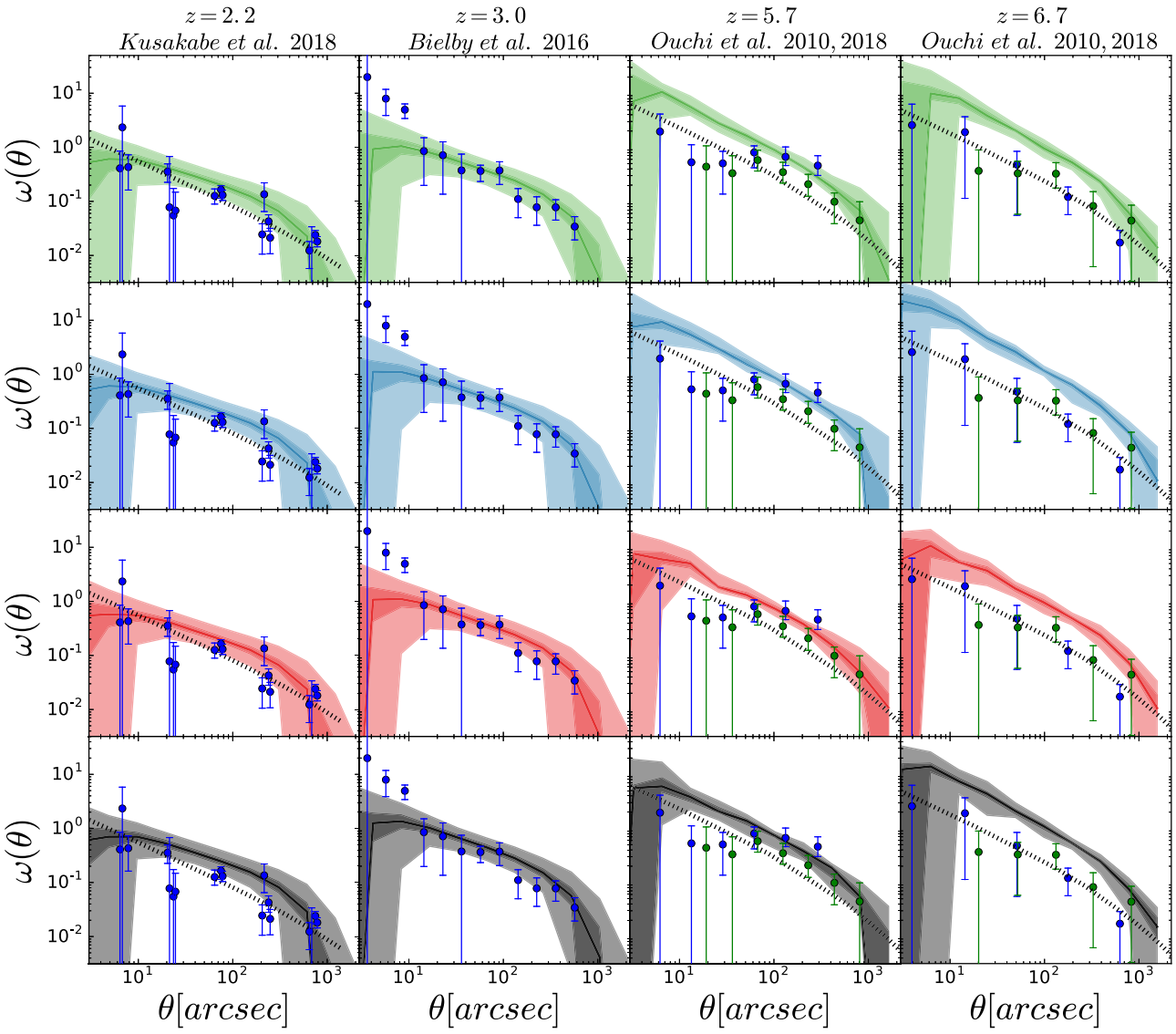

Figure 10. Comparison between different model mocks (*Thin Shell*, *Wind*, *Bicone*, and AM-noRT in rows from top to bottom) and the observed 2-point projected correlation function (Ouchi et al. 2010, 2018; Bielby et al. 2016; Kusakabe et al. 2018) at redshifts 2.2, 3.0, 5.7, and 6.7 in each column from left to right. The observational data are shown by dots and the best-fitting power law $\omega(\theta)$ extracted from their original work are plotted as dashed black lines. The solid lines correspond to the median $\omega(\theta)$ for the mocks and the darker and lighter shades to the 32–68 and 5–95 percentiles, respectively.

comparison with the scatter due to cosmic variance, making all models indistinguishable from each other.

At redshifts 2.2 and 3.0 there is a good agreement between the the mocks and the clustering measurements in Kusakabe et al. (2018) and Bielby et al. (2016), respectively. At higher redshifts the LAE clustering predicted by the mocks is overestimated in our models. In particular, at $z = 5.7$, for angular distances $\theta < 50$ arcsec, $\omega_{\rm mock}$ overestimates the clustering, while at larger θ the mocks match very well $\omega_{\rm survey}$. Additionally, at redshift 6.7 the $\omega_{\rm mock}$ bias is significantly (about 2σ) overestimated in comparison

Table 4. Fraction of shared galaxies between pairs of models at the same redshift.

z	Model	Thin shell	Wind	Bicone	AM-noRT
2.2	Thin shell	1.000	0.814	0.555	0.229
	Wind	0.814	1.000	0.592	0.189
	Bicone	0.555	0.592	1.000	0.197
	AM-noRT	0.229	0.189	0.197	1.000
3.0	Thin shell	1.000	0.805	0.401	0.188
	Wind	0.805	1.000	0.427	0.151
	Bicone	0.401	0.427	1.000	0.227
	AM-noRT	0.188	0.151	0.227	1.000
5.7	Thin shell	1.000	0.413	0.798	0.108
	Wind	0.413	1.000	0.322	0.063
	Bicone	0.798	0.322	1.000	0.160
	AM-noRT	0.108	0.063	0.160	1.000
6.7	Thin shell	1.000	0.354	0.663	0.104
	Wind	0.354	1.000	0.229	0.076
	Bicone	0.663	0.229	1.000	0.259
	AM-noRT	0.104	0.076	0.259	1.000

with $\omega_{\rm survey}$. This discrepancy could be caused by multiple reasons. The moderate contamination of interlopers (∼10 per cent) in the Ouchi et al. (2010) sample could decrease the measured clustering amplitude. Also, the observed LAE population at this redshift might contain a significant contribution of objects at the mass resolution limit of our `galform` galaxies ($M_{\rm halo,min} \approx 10^{10}[\,{\rm M}_\odot\,{\rm h}^{-1}]$, see Section 2.3), thus making our predictions biased towards higher masses and clustering amplitudes. In fact, we have checked that about a 10 per cent of the LAE in our different samples have halo masses below $10^{10.5}[\,{\rm M}_\odot\,h^{-1}]$.

5 DISCUSSION

Here we discuss some of the results found in previous sections. In particular, in sub-section 5.1 we discuss how the different outflow geometries impact the predicted properties of the LAE populations. Then, in subsections 5.2 and 5.3 we discuss the limitations of our methodology.

5.1 Differences between the RT models

In this work we have used three different gas outflow geometries (*Thin Shell*, spherical galactic wind, and biconical galactic wind) to model the Lyα radiative transfer inside galaxies. The galaxy properties predicted for LAEs are very similar. The only significant difference between the predictions of different geometries is on the required distributions of column density and expansion velocity.

In Table 4 we list the fraction of galaxies shared by pairs of LAE models imposing ${\rm EW}_0 > 20$ Å and a number density cut of $10^{-3}\,h^3\,{\rm cMpc}^{-3}$. We find that the *Wind* and *Thin Shell* geometries share a high fraction of galaxies (∼80 per cent) at redshifts 2.2 and 3.0. However, at high redshift these geometries select different galaxies as the shared fraction in relatively low (∼40 per cent overlap). This might be due to the fact that there is a necessity of $f_{\rm esc}^{\rm Ly\alpha} \sim 1$ and the recipes to compute $N_{\rm H_I}$ and $V_{\rm exp}$ are different. However, quite the opposite relation is seen between the *Thin Shell* and *Bicone*, as at low redshift they share a relatively low percentage of galaxies (∼45 per cent) and this increase at higher redshifts (∼70 per cent).

Finally, when comparing the galaxies in the *Wind* and *Bicone* geometry, we surprisingly find a low overlap between them. In particular, the maximum overlap happens at $z = 2.2$ (∼55 per cent) and it drops down to only ∼20 per cent at $z = 6.7$. This shows the impact of the gas geometry on how the RT shapes the LAE selection function; even though the intrinsic galaxy population and the recipes to derive $N_{\rm H}$ and $V_{\rm exp}$ are the same, the two geometries predicts different populations (although with similar characteristics).

We conclude that the RT LAE samples, in general, share a big fraction of galaxies (≥ 50 per cent) although the implemented gas geometries are very different. This is due to the fact that $f_{\rm esc}^{\rm Ly\alpha}$ behaves similarly for all of them. In particular, even if the exact dependence is different for each geometry, decreasing $N_{\rm H}$, increasing $V_{\rm exp}$, and decreasing $\tau_{\rm a}$ increase $f_{\rm esc}^{\rm Ly\alpha}$, thus the visibility of the object for all of them. This makes the RT LAE samples very similar, as galaxies with properties that maximize $L_{\rm Ly\alpha}$ and $f_{\rm esc}^{\rm Ly\alpha}$ are selected.

5.2 Limitations of the simple AM-noRT model

We have also used a very simplistic LAE model where radiative transfer effects are not taken into account and $L_{\rm Ly\alpha}$ depends monotonically on the SFR. In Table 4 we also list the overlap between the radiative transfer and AM-noRT LAE sample. We find that the fraction of galaxies shared between the AM-noRT and RT catalogues is low, reaching its maximum value at $z = 2.2$ (∼20 per cent) and then decreasing to ∼7 per cent at redshift 6.7.

As shown in Fig. 7 the AM-noRT sample fails to match not only the observed $f_{\rm esc}^{\rm Ly\alpha}-$SFR and $f_{\rm esc}^{\rm Ly\alpha}-M_*$ relations but also the overall trend where $f_{\rm esc}^{\rm Ly\alpha}$ anticorrelates with these two properties due to the RT (as described above). Additionally, the dark matter halo population, and thus the clustering, is different in comparison with the RT samples.

This work highlights the importance of taking into account the Lyα RT inside galaxies when modeling LAEs. In particular, unlike in RT LAE samples, the galaxy properties model AM-noRT differ from observations, making them less attractive to study galaxy formation and evolution.

5.3 Limitations of the RT models

The IGM impact on Lyα detection is still unclear. However, some works have explored that the IGM plays a major role in the detectability of galaxies based on Lyα flux (Dijkstra et al. 2006; Zheng et al. 2011; Behrens et al. 2017). The IGM opacity becomes more important at higher redshifts (∼7) where the universe is denser and colder. However, the IGM might already also have an impact on the LAE selection function at $z = 2.2$ as, even if the universe is highly ionized, the cross-section of neutral hydrogen atoms for scattering Lyα photons is very high. The IGM impact might alleviate some of the tension that we find when we compare LAE models with observations. We will implement the effect of the IGM opacity in future work.

In Fig. 7 we found that, although the observed $f_{\rm esc}^{\rm Ly\alpha}-$SFR relation is perfectly reproduced by our RT models, the $f_{\rm esc}^{\rm Ly\alpha}-{\rm M}_*$ relation is not. Even if the overall trend is similar, we find a significant difference (about 0.5 dex) in the stellar mass. This is probably not caused by our implementation of RT in a semi-analytic model, but by `galform` itself, as we note that full `galform` $M_{\rm h} - M_*$ relation at redshift 3.0 is overestimated (also about 0.5 dex) in comparison with the observed one (Behroozi, Conroy & Wechsler 2010). Another possible source for this discrepancy is the different

stellar population synthesis models used by Oyarzún et al. (2017) and `galform`.

Another limitation of the RT models is that they predict very similar galaxy properties for the three different geometries. This degeneracy makes it difficult to determine from observations which geometry is the one driving the Lyα photons escape. Nonetheless, the three gas geometries used in this work have very different Lyα line profiles (as shown in fig. 2) that might break the degeneracies and lead to a better understanding of the escape channels of Lyα radiation. We will implement line profiles in an upcoming work.

6 CONCLUSIONS AND FUTURE WORK

Lyman-α emitters are a promising galaxy population to trace the large-scale structure of the Universe at high redshifts, $z \gtrsim 2$. One of the main advantages of LAEs is their high luminosity at the Lyα rest frame wavelength, making them easy to detect. Additionally, due to the Hubble expansion (Hubble 1929), the Lyα line is observable in the optical from $z \sim 2$ to ∼7, allowing ground-based measurement of these galaxies. However, their selection function is quite complex as it depends upon Lyα radiative transfer, which is sensitive to local astrophysical conditions.

We have designed a theoretical model of LAE based on a Monte Carlo Radiative Transfer code that can be applied to huge cosmological volumes. In particular, we have applied our model the *N*-body only-dark-matter simulation `P-Millennium` and the semi-analytical model of galaxy formation and evolution `galform` (Lacey et al. 2016).

Monte Carlo Radiative Transfer codes have demonstrated to be a powerful tool to understand how Lyα photons escape from galaxies. Unfortunately, the high computational cost prohibits the capability of being directly run over cosmological volumes. In order to avoid this problem, we have developed analytical expressions for the Lyα escape fraction $f_{\rm esc}^{\rm Ly\alpha}$ that are quite accurate for a wide range of outflow expansion velocities $V_{\rm exp}$, neutral hydrogen column densities $N_{\rm H}$ and metallicities Z.

Our methodology computes $f_{\rm esc}^{\rm Ly\alpha}$ for each galaxy as a function of Z, $V_{\rm exp}$, and $N_{\rm H_I}$, which characterize the gas outflows from which Lyα photons escape. We compute these quantities using galaxy properties such as the size, SFR, or halo mass. Free parameters to compute these quantities are chosen to fit the observed luminosity function over a wide range of redshifts. After calibration we find that every geometry reproduces well the observed LAEs LF at low redshift while only the *Thin Shell* and *Wind* manage to match them at high redshift. We conclude that our *Bicone* geometry (as described in this work), at high redshift, is less favored with respect to the others. In a future work we will redesign this geometry by making it more realistic and including a dependence in the $f_{\rm esc}^{\rm Ly\alpha}$ and other properties with the LoS.

We have analyzed the relative abundance of Lyα emitters by breaking down their LF in terms of several properties. Halo or stellar masses are not significantly correlated with Lyα luminosities. The LF is actually mostly dominated by relatively low mass galaxies. However, when the LF is split in SFR bins we find a clear positive correlation with Lyα luminosity. Finally, when the LF is divided into metallicity bins we find a scattered correlation for $\log(Z) < -2$. Moreover, the contribution of high metallicities ($\log(Z) > -2$) to the bright end of the LF is small.

We also compared the properties of a Lyα selected sample to the bulk of the galaxy population at high redshifts. We find that LAEs lie in relatively low mass haloes. Additionally, the galaxies with the strongest starburst episodes are not selected as LAE since these galaxies typically have higher metallicities, and thus their $f_{\rm esc}^{\rm Ly\alpha}$ is low.

To validate our predicted $f_{\rm esc}^{\rm Ly\alpha}$, we have compared our LAE samples to the observational data from Oyarzún et al. (2017). We find a remarkable good agreement between our predictions and the observationally measured $f_{\rm esc}^{\rm Ly\alpha}$ – SFR relation. The LAE samples including RT reproduce successfully this anticorrelation and the scatter found between these quantities. However, the predicted $f_{\rm esc}^{\rm Ly\alpha}$ – M_* plane is offset by ∼0.5 dex in M_* with respect to the data from Oyarzún et al. (2017). This difference can be due to the different assumptions about the stellar population synthesis models used by Oyarzún et al. (2017) and `galform`, the impact of a different IMF in `galform`, or simply that `galform` predicts significantly more massive star-forming galaxies at these higher redshifts with respect to observational estimates.

Finally, we find that our LAE AM-noRT sample based on assuming a monotonic relation between SFR and $L_{\rm Ly\alpha}$ is not able to reproduce any of the observed trends. This highlights the crucial role of RT in shaping the LAE selection function.

We have also studied the dark matter halo population hosting LAEs in our models. We find differences between the samples including RT and the sample without RT. At low redshift, in comparison with the AM-noRT, the RT models predict lower mass dark matter haloes host LAE. This trend reverses at high redshift, as LAEs lie in more massive haloes in the RT samples. We also find that the satellite fraction is low at all redshifts (∼2 per cent) and similar for all of the model variants.

The difference in the DM halo populations is directly translated into clustering discrepancies between the AM-noRT and RT samples. At low redshift, as a consequence of LAEs modeled with RT lying in lower mass DM haloes, we find that they have a lower galaxy bias than the AM-noRT sample. This trend is reversed at high redshifts, when RT LAEs lie in more massive dark matter haloes. Thus, we find that the RT models have a steeper galaxy bias evolution than the model excluding RT.

Finally, we have compared our model clustering predictions with observations finding some tension. While at redshifts 2.2 and 5.7 the observed clustering is well reproduced, at redshifts 3.0 and 6.7 the galaxy bias is poorly constrained. Although the impact of the intergalactic medium on Lyα is not very clear, previous works (Zheng et al. 2011) indicate that the IGM transmission could have an impact on Lyα selected samples that might alleviate this tension.

We have demonstrated the importance of RT in shaping the selection function of LAEs for galaxy properties as metallicity, SFR, or DM halo properties. On one hand, the peculiar observational trends found cannot be reproduced with a simple monotonic relation between SFR and $L_{\rm Ly\alpha}$. On the other hand, the inclusion of RT changes in a very particular way the clustering of Lyα selected samples. All this makes extremely important to construct models with Lyα RT in order to understand the galaxy properties, formation, and evolution of LAEs. Moreover, future surveys tracing the large-scale structure of the Universe through LAEs will require a deep understanding of the channels through which Lyα photons escape in order to obtain unbiased cosmological constrains.

In future work we plan to implement the transmission of Lyα photons through the IGM, which is especially important at high redshifts. In order to do so, we will develop analytic expression for the Lyα line profile and a model to compute the IGM transmission in large cosmological volumes. These tools will enable us to explore how the IGM shapes the LAE galaxy properties and clustering.

ACKNOWLEDGEMENTS

The authors acknowledge the useful discussions with Zheng Zheng, Mark Dijkstra, and Anne Verhamme in addition to the whole CEFCA team. We also thank Grecco Oyarzun for making their observational data available to us. The authors also acknowledge the support of the Spanish Ministerio de Economiaa y Competividad project No. AYA2015-66211-C2-P-2. We acknowledge also STFC Consolidated Grants ST/L00075X/1 and ST/P000451/1 at Durham University. This work used the DiRAC Data Centric system at Durham University, operated by the Institute for Computational Cosmology on behalf of the STFC DiRAC HPC Facility (www.dirac.ac.uk). This equipment was funded by BIS National E-infrastructure capital grant ST/K00042X/1, STFC capital grants ST/H008519/1 and ST/K00087X/1, STFC DiRAC Operations grant ST/K003267/1, and Durham University. DiRAC is part of the National E-Infrastructure.

REFERENCES

Ahn S., 2003, J. Korean Astron. Soc., 36, 145
Ahn S.-H., 2004, ApJ, 601, L25
Ahn S.-H., Lee H.-W., Lee H. M., 2000, J. Korean Astron. Soc., 33, 29
Barnes L. A., Haehnelt M. G., 2010, MNRAS, 403, 870
Baugh C. M., 2006, Rep. Prog. Phys., 69, 3101
Baugh C. M., Lacey C. G., Frenk C. S., Granato G. L., Silva L., Bressan A., Benson A. J., Cole S., 2005, MNRAS, 356, 1191
Baugh C. M. et al., 2019, Galaxy formation in the Plank Millenium: the atomic hydrogen content of dark matter halos, 485, 4922
Behrens C., Byrohl C., Saito S., Niemeyer J. C., 2018, A&A, 614, A31
Behroozi P. S., Conroy C., Wechsler R. H., 2010, ApJ, 717, 379
Benitez N. et al., 2014, preprint (arXiv:1403.5237)
Bielby R. M. et al., 2016, MNRAS, 456, 4061
Bower R. G., Benson A. J., Malbon R., Helly J. C., Frenk C. S., Baugh C. M., Cole S., Lacey C. G., 2006, MNRAS, 370, 645
Cassata P. et al., 2011, A&A, 525, A143
Cazzoli S., Arribas S., Maiolino R., Colina L., 2016, A&A, 590, A125
Chisholm J., Orlitová I., Schaerer D., Verhamme A., Worseck G., Izotov Y. I., Thuan T. X., Guseva N. G., 2017, A&A, 605, A67
Cole S., Lacey C. G., Baugh C. M., Frenk C. S., 2000, MNRAS, 319, 168
Dayal P., Maselli A., Ferrara A., 2011, MNRAS, 410, 830
Dijkstra M., 2017, preprint (arXiv:1704.03416)
Dijkstra M., Haiman Z., Spaans M., 2006, ApJ, 649, 14
Dijkstra M., Mesinger A., Wyithe J. S. B., 2011, MNRAS, 414, 2139
Foreman-Mackey D., Hogg D. W., Lang D., Goodman J., 2013a, PASP, 125, 306
Foreman-Mackey D., Hogg D. W., Lang D., Goodman J., 2013b, PASP, 125, 306
Garel T., Blaizot J., Guiderdoni B., Schaerer D., Verhamme A., Hayes M., 2012, MNRAS, 422, 310
Garel T., Blaizot J., Guiderdoni B., Michel-Dansac L., Hayes M., Verhamme A., 2015, MNRAS, 450, 1279
Gawiser E. et al., 2007, ApJ, 671, 278
Granato G. L., Lacey C. G., Silva L., Bressan A., Baugh C. M., Cole S., Frenk C. S., 2000, ApJ, 542, 710
Gronke M., Dijkstra M., McCourt M., Oh S. P., 2016, ApJ, 833, L26
Guaita L. et al., 2010, ApJ, 714, 255
Guaita L. et al., 2017, A&A, 606, A19
Hagen A. et al., 2014, ApJ, 786, 59
Harrington J. P., 1973, MNRAS, 162, 43
Hill G. J. et al., 2008, in Kodama T., Yamada T., Aoki K., eds, ASP Conf. Ser. Vol. 399, Panoramic Views of Galaxy Formation and Evolution. Astron. Soc. Pac., San Francisco, p. 115
Hubble E., 1929, Proc. Natl. Acad. Sci., 15, 168
Hu E. M., Cowie L. L., McMahon R. G., 1998, ApJ, 502, L99
Inoue A. K. et al., 2018, PASJ, 70, 55
Jose C., Srianand R., Subramanian K., 2013, MNRAS, 435, 368
Kashikawa N. et al., 2006, ApJ, 648, 7
Kennicutt R. C., Jr, 1983, ApJ, 272, 54
Kobayashi M. A. R., Totani T., Nagashima M., 2007, ApJ, 670, 919
Konno A. et al., 2018, PASJ, 70, S16
Konno A., Ouchi M., Nakajima K., Duval F., Kusakabe H., Ono Y., Shimasaku K., 2016, ApJ, 823, 20
Kulas K. R., Shapley A. E., Kollmeier J. A., Zheng Z., Steidel C. C., Hainline K. N., 2011, in American Astronomical Society Meeting Abstracts 216
Kusakabe H. et al., 2018, PASJ
Lacey C. G. et al., 2016, MNRAS, 462, 3854
Laursen P., Sommer-Larsen J., 2007, ApJ, 657, L69
Laursen P., Razoumov A. O., Sommer-Larsen J., 2009, ApJ, 696, 853
Laursen P., Sommer-Larsen J., Razoumov A. O., 2011, ApJ, 728, 52
Le Delliou M., Lacey C., Baugh C. M., Guiderdoni B., Bacon R., Courtois H., Sousbie T., Morris S. L., 2005, MNRAS, 357, L11
Le Delliou M., Lacey C. G., Baugh C. M., Morris S. L., 2006, MNRAS, 365, 712
Malhotra S., Rhoads J. E., 2002, ApJ, 565, L71
Mitchell P. D., Lacey C. G., Baugh C. M., Cole S., 2013, MNRAS, 435, 87
Nagamine K., Ouchi M., Springel V., Hernquist L., 2010, PASJ, 62, 1455
Nelson D. et al., 2015, Astron. Comput., 13, 12
Neufeld D. A., 1990, ApJ, 350, 216
Orsi Á. A., Angulo R. E., 2018, MNRAS, 475, 2530
Orsi A., Lacey C. G., Baugh C. M., 2012, MNRAS, 425, 87
Orsi A., Lacey C. G., Baugh C. M., Infante L., 2008, MNRAS, 391, 1589
Osterbrock D. E., 1989, Astrophysics of Gaseous Nebulae and Active Galactic Nuclei. University Science Books, Sausalito, California
Ouchi M. et al., 2008, ApJS, 176, 301
Ouchi M. et al., 2010, ApJ, 723, 869
Ouchi M. et al., 2018, PASJ, 70, S13
Oyarzún G. A., Blanc G. A., González V., Mateo M., Bailey J. I., III, 2017, ApJ, 843, 133
Planck CollaborationXIII, 2016, A&A, 594, A13
Rhoads J. E., Malhotra S., Dey A., Stern D., Spinrad H., Jannuzi B. T., 2000, ApJ, 545, L85
Santos M. R., Ellis R. S., Kneib J., Richard J., Kuijken K., 2004, ApJ, 606, 683
Schaerer D., Verhamme A., 2008, A&A, 480, 369
Shapley A. E., Steidel C. C., Pettini M., Adelberger K. L., 2003, ApJ, 588, 65
Sobral D. et al., 2017, MNRAS, 466, 1242
Steidel C. C., Giavalisco M., Pettini M., Dickinson M., Adelberger K. L., 1996, ApJ, 462, L17
Steidel C. C., Erb D. K., Shapley A. E., Pettini M., Reddy N., Bogosavljević M., Rudie G. C., Rakic O., 2010, ApJ, 717, 289
Steidel C. C., Bogosavljević M., Shapley A. E., Kollmeier J. A., Reddy N. A., Erb D. K., Pettini M., 2011, ApJ, 736, 160
Taniguchi Y. et al., 2005, PASJ, 57, 165
Verhamme A., Schaerer D., Maselli A., 2006, A&A, 460, 397
Wang Y. et al., 2018, preprint (arXiv:1802.01539)
Zheng Z., Miralda-Escudé J., 2002, ApJ, 578, 33
Zheng Z., Wallace J., 2014, ApJ, 794, 116
Zheng Z., Cen R., Trac H., Miralda-Escudé J., 2010, ApJ, 716, 574
Zheng Z., Cen R., Trac H., Miralda-Escudé J., 2011, ApJ, 726, 38

APPENDIX A: FURTHER DETAILS ABOUT THE BICONE GEOMETRY

In general, $f_{\rm esc}^{{\rm Ly}\alpha}$ can be defined for an arbitrary angular aperture $\Delta\gamma$ as

$$f_{\rm esc}^{{\rm Ly}\alpha}(\Delta\gamma) = \frac{N_{\rm escaped}(\Delta\gamma)}{N_{\rm emitted}(\Delta\gamma)}, \quad \text{(A1)}$$

where $N_{\rm emitted}(\Delta\gamma)$ is the number of photons emitted towards the aperture $\Delta\gamma$ and $N_{\rm escaped}(\Delta\gamma)$ is the number of photons that escape through that set of directions. Note that for the thin shell and the

non-biconical galactic wind this expression is valid and $\Delta\gamma$ is every direction (4π).

The bicone geometry is not spherical symmetry, thus its $f_{\rm esc}^{\rm Ly\alpha}$ depends on the line of sight. In the case of the bicone, the escape fraction presented in our work corresponds to the $f_{\rm esc}^{\rm Ly\alpha}(\Delta\gamma_b)$, where $\Delta\gamma_b$ is the angular aperture $\theta < \pi/4 \cup \theta > 3\pi/4$ and $\phi \in [0, 2\pi)$. In other words, we define the biconical escape fraction as the number of photons that escape through the bicone divided by the number of photons emitted towards the bicone. We checked that the escape fraction within $\Delta\gamma_b$ does not change. Meanwhile, the escape fraction within $4\pi - \Delta\gamma_b$ is also constant and considered $\sim$0.

In this formalism, the total escape fraction (taking into account ever possible line of sight) would be

$$f_{\rm esc}^{\rm Ly\alpha}(\Delta\gamma = 4\pi) = \frac{N_{\rm escaped}(\Delta\gamma_b) + N_{\rm escaped}(4\pi - \Delta\gamma_b)}{N_{\rm emitted}(\Delta\gamma = 4\pi)}, \quad \text{(A2)}$$

where the aperture $\Delta\gamma = 4\pi - \Delta\gamma_b$ encapsulates every line of sight outside the bicone. Then, if we assume that no photon escapes outside the bicone, i.e, $N_{\rm escaped}(4\pi - \Delta\gamma_b) = 0$,

$$f_{\rm esc}^{\rm Ly\alpha}(\Delta\gamma = 4\pi) = \frac{N_{\rm escaped}(\Delta\gamma_b)}{N_{\rm emitted}(\Delta\gamma = 4\pi)}, \quad \text{(A3)}$$

where if we assume that the photon emission is isotropic

$$f_{\rm esc}^{\rm Ly\alpha}(\Delta\gamma = 4\pi) = \frac{N_{\rm escaped}(\Delta\gamma_b)}{N_{\rm emitted}(\Delta\gamma_b)4\pi/\Delta\gamma_b} = f_{\rm esc}^{\rm Ly\alpha}(\Delta\gamma_b) \times \frac{\Delta\gamma_b}{4\pi}. \quad \text{(A4)}$$

Note that, by construction, in our bicone implementation, $f_{\rm esc}^{\rm Ly\alpha}(\Delta\gamma = 4\pi) \leq \Delta\gamma_b/4\pi$, even when the dust content of the bicone is null. This is caused by the dusty optical thick disc in the plane perpendicular to the bicone axis. The disc absorbs every photon that enters into it. This includes (i) photons sent directly by the source and (ii) photons that are initially emitted towards the bicone, bound in its surface and end up in the disc. In this way, only when the bicone neutral hydrogen column density is 0, then $f_{\rm esc}^{\rm Ly\alpha}(\Delta\gamma = 4\pi) = \Delta\gamma_b/4\pi$.

To include the angular dependence of $f_{\rm esc}^{\rm Ly\alpha}$ we should (i) assign a random orientation to every galaxy in our simulation and (ii) compute the observed luminosity taking into account the orientation, i.e.

$$L_{\rm Ly\alpha}(\Delta\gamma) = L^0_{\rm Ly\alpha} \times f_{\rm esc}(\Delta\gamma), \quad \text{(A5)}$$

where $\Delta\gamma = \Delta\gamma_b$ when the bicone is pointing towards the observer and $\Delta\gamma = 4\pi - \Delta\gamma_b$ when the line of sight does not go through the outflow.

By construction, a fraction of $1 - \Delta\gamma_b/4\pi$ galaxies would be seen through the optical thick disc and be assigned $f_{\rm esc}^{\rm Ly\alpha}(4\pi - \Delta\gamma_b) \sim 0$. This would decrease the number counts to LAEs too much in comparison with current observations. To counterbalance this, we assigned $f_{\rm esc}^{\rm Ly\alpha}(\Delta\gamma_b) \sim 0$ to every galaxy, thus

$$L_{\rm Ly\alpha} = L^0_{\rm Ly\alpha} \times f_{\rm esc}^{\rm Ly\alpha}(\Delta\gamma_b). \quad \text{(A6)}$$

This imposes that the biconical outflow of every galaxy is pointing to the observer. Therefore our biconical model is an upper limit of the bicone geometry presented in this work. We are aware that this introduces some limitations in the conclusions of the bicone geometry, but the other two geometries are not affected by this. We plan to implement in a future work an improved biconical geometry and the angle dependence of its $f_{\rm esc}^{\rm Ly\alpha}$.

APPENDIX B: VALIDATING THE $f_{\rm esc}^{\rm Ly\alpha}$ FITTING FORMULAE

A direct comparison between the Monte Carlo radiative transfer (MCRT) code output and/or $f_{\rm esc}^{\rm Ly\alpha}$ model for the *Thin Shell* geometry is shown in Fig. B3, for the galactic wind in Fig. B4, and for the *Bicone* in Fig. B5. These figures are divided in eight panels subdivided in another two: (a) escape fraction versus dust optical depth and (b) the relative difference between our model and the radiative transfer code output. In panels (a) the output of the radiative transfer code for a fixed $N_{\rm H}$ is plotted with $V_{\rm exp}$ colour coded in solid lines with their respective errors (same colored shade region) computed using equation (6) and our $f_{\rm esc}^{\rm Ly\alpha}$ model is plotted in black solid lines. In type (b) panels we show the relative difference between our model and the MCRT code with the same colour code than above.

In general, the performance of our model decreases with τ_a, this is because, as discussed above, decreasing $f_{\rm esc}^{\rm Ly\alpha}$ increases the errors. This disagreement, in some cases, leads to an overestimation of $f_{\rm esc}^{\rm Ly\alpha}$ when its true value is $\lesssim$0.01. For our work, these low values are very rare and so do not affect our results. Overall, we find that the typical discrepancies are below 10 per cent and 1 per cent for $\log\tau_a < -0.5$ and <-1.0, respectively.

Our model for the *Thin Shell* $f_{\rm esc}^{\rm Ly\alpha}$ is able to reproduce the whole velocity range of our grid for $N_{\rm H} < 10^{19.5}$ cm^{-2}, reaching a 99 per cent accuracy in most cases.

Our $f_{\rm esc}^{\rm Ly\alpha}$ model using the *Wind* geometry is also able to reproduce the output of our radiative transfer code through most of the parameter, only failing at very high $N_{\rm H}$ and low $V_{\rm exp}$ combinations, where $f_{\rm esc}^{\rm Ly\alpha}$ <0.1. As in the *Thin Shell* geometry, our model behaves better for $N_{\rm H} > 10^{19.5}$ cm^{-2}. In particular, in most of out grid, the disagreement is lower than 10 per cent and for low $\tau_a < -1$ the typical agreement is 1 per cent.

The *Bicone* geometry is more complex than the other geometries, and its $f_{\rm esc}^{\rm Ly\alpha}$ model has the worst performance of all. However, for most of the grid the model is within 10 per cent errors. As explained in Section 2, the maximum $f_{\rm esc}^{\rm Ly\alpha}$ depends on the properties of the outflowing gas, causing that only systems with very low optical depth (low $N_{\rm H}$ and/or high $V_{\rm exp}$) manage to reach $f_{\rm esc}^{Ly\alpha} = 1$. This also causes that in very optically thick systems $f_{\rm esc}^{\rm Ly\alpha}$ reaches 0.001 (even if there is no dust). We decided not to include $N_{\rm H} = 10^{22.5}$ cm^{-2} in our model because the maximum value of $f_{\rm esc}^{\rm Ly\alpha}$ at $V_{\rm exp} = 1000$ km s^{-1} would be about 0.01 and, as discussed above, it is unnecessary to reproduce such low values.

We show the distribution of dust optical depth τ_a against $V_{\rm exp}$ (Fig. B1) and $N_{\rm H}$ (Fig. B2) for our RT LAE samples (selected as in Section 4.1) at redshifts 2.2, 3.0, 5.7, and 6.7 from left to right. At redshifts 2.2 and 3.0 the *Wind* and *Thin Shell* τ_a distributions are very similar in width and centre ($\log\tau_a \sim -2$) while the *Bicone* model predict $\log\tau_a \sim -3$. Since the *Bicone* $f_{\rm esc}^{\rm Ly\alpha}$ exhibits an upper limit <1, it requires low column densities (see Fig. 4) and Z, thus low τ_a values. At high redshifts (5.7 and 6.7) the dust optical depth distributions for the three geometries are very similar and peak at $\log\tau \sim -3$. In addition to the bulk of the distribution, the *Thin Shell* and *Wind* geometries also present a small bump around $\log\tau \sim -0.5$. Finally, we have checked that the fraction of galaxies in our LAE samples is < 2 per cent for all the configurations studied in this work.

In Fig. B1 we explore the evolution in redshift of the $\tau_a - V_{\rm exp}$ distributions of our LAE samples. While at low redshift ($z = 2.2$, 3.0) the three geometries occupy different regions in this plane, they merge at higher redshifts ($z = 5.7$, 6.7). At all redshifts the *Bicone*

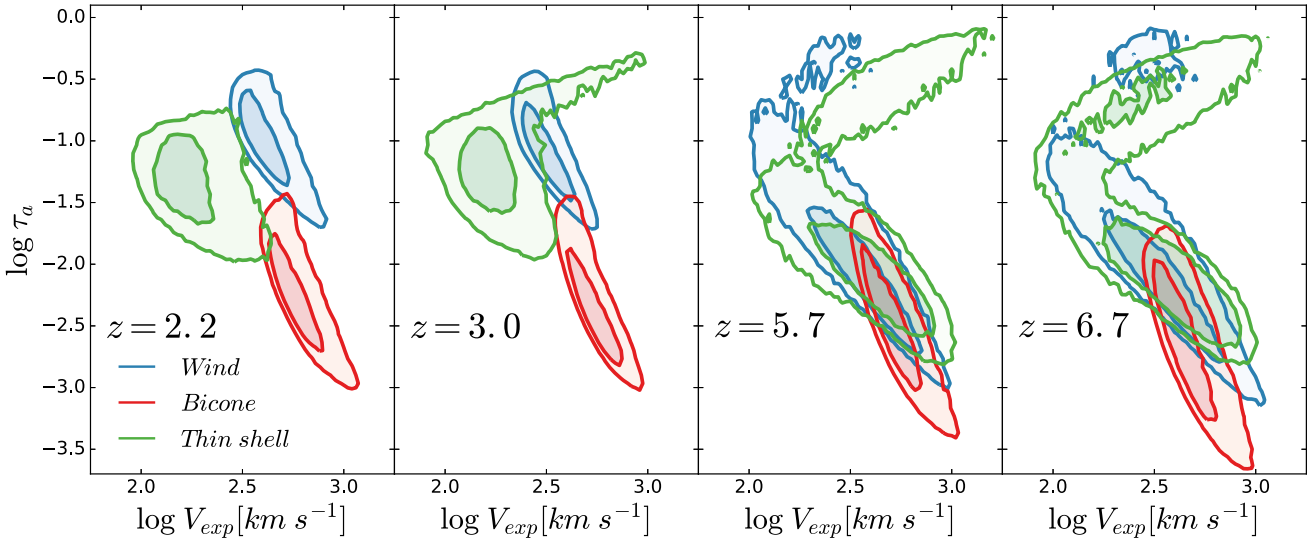

Figure B1. Same as Fig. 4 but displaying the dust optical depth τ_a and expansion velocity $V_{\rm exp}$ for the LAE samples with RT.

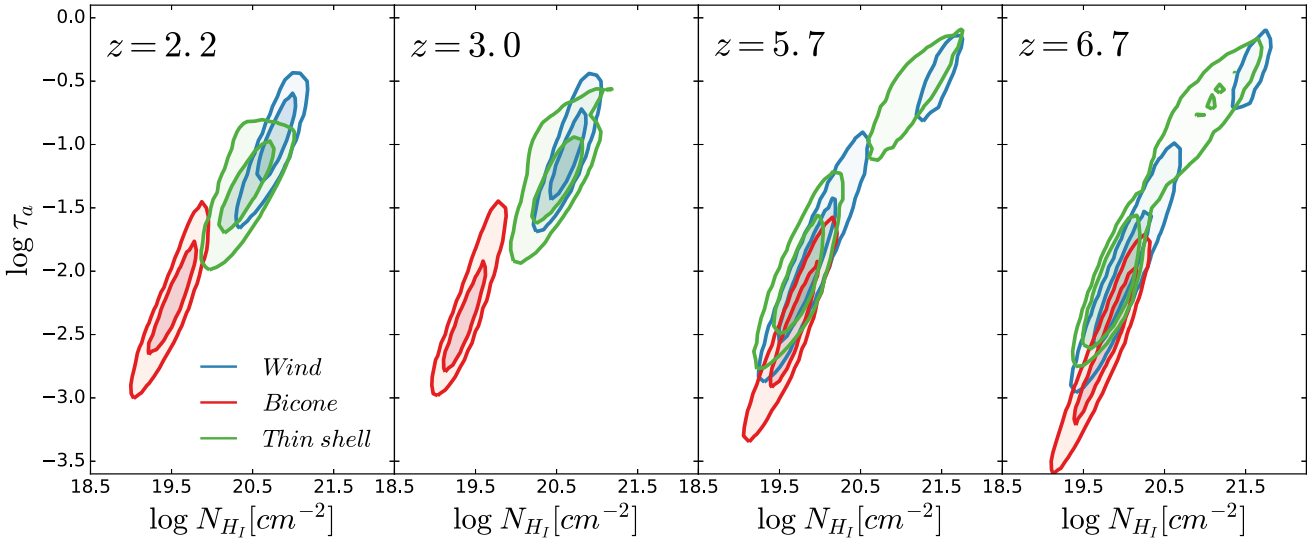

Figure B2. Same as Fig. 4 but displaying the dust optical depth τ_a and neutral hydrogen column density $N_{\rm H}$ for the LAE samples with RT.

needs the lowest τ_a possible as the typical $f_{\rm esc}^{\rm Ly\alpha}$ in this geometry is very low. In the case of the *Thin Shell* and *Wind* the distribution passes from compact at low redshift to bimodal as also studied in Fig. 4 and explained in Section 4.1.

In Fig. B2 we explore the evolution in redshift of the $\tau_a - N_{\rm H}$ distributions of our LAE samples. We see a clear correlation between these two quantities at all redshifts that is driven by equation (9). Additionally, we see the dame behaviour of $N_{\rm H}$ as in Section 4.1.

In order to compare our clustering predictions with observations, we construct mock catalogs that mimic the properties of several surveys at different redshifts. In general, there are several options for building mock catalogues to measure clustering.

The first one, for example, is to use the same selection criteria (flux depth, equivalent width cut, etc.) than the observed samples. This first option is useful if all the properties used in the selection criteria are well reproduced by the models.

The LAE surveys studied in this work are limited by $L_{\rm Ly\alpha} > L_{\rm Ly\alpha,cut}$ and $\rm EW_0 > EW_{0,cut}$. In general $L_{\rm Ly\alpha,cut}$ and $\rm EW_{0,cut}$ are different for every survey. These values are listed in Table B1.

Our models are designed so they reproduce the abundance and luminosity distribution LAEs as we force them to fit, as good as possible, the observed LF at different redshifts. In detail, we combine different observations of the Lyα LF at the same redshift in order to calibrate our models. Because of this, the surveys that we use to study the clustering and calibrate our models, in general, use different selection criteria or the source sample is different. This could lead to discrepancies in the predicted number density of sources by our models imposing the clustering studies restrictions and the observed abundance of sources in these ones.

In particular, at $z = 2.2$ the survey constraining the clustering (Kusakabe et al. 2018) is, at least, partially included in one of the surveys used to calibrate the LF (Konno et al. 2016). Additionally, $\rm EW_{0,cut}$ is the same for all the surveys used to fit the LF (Cassata

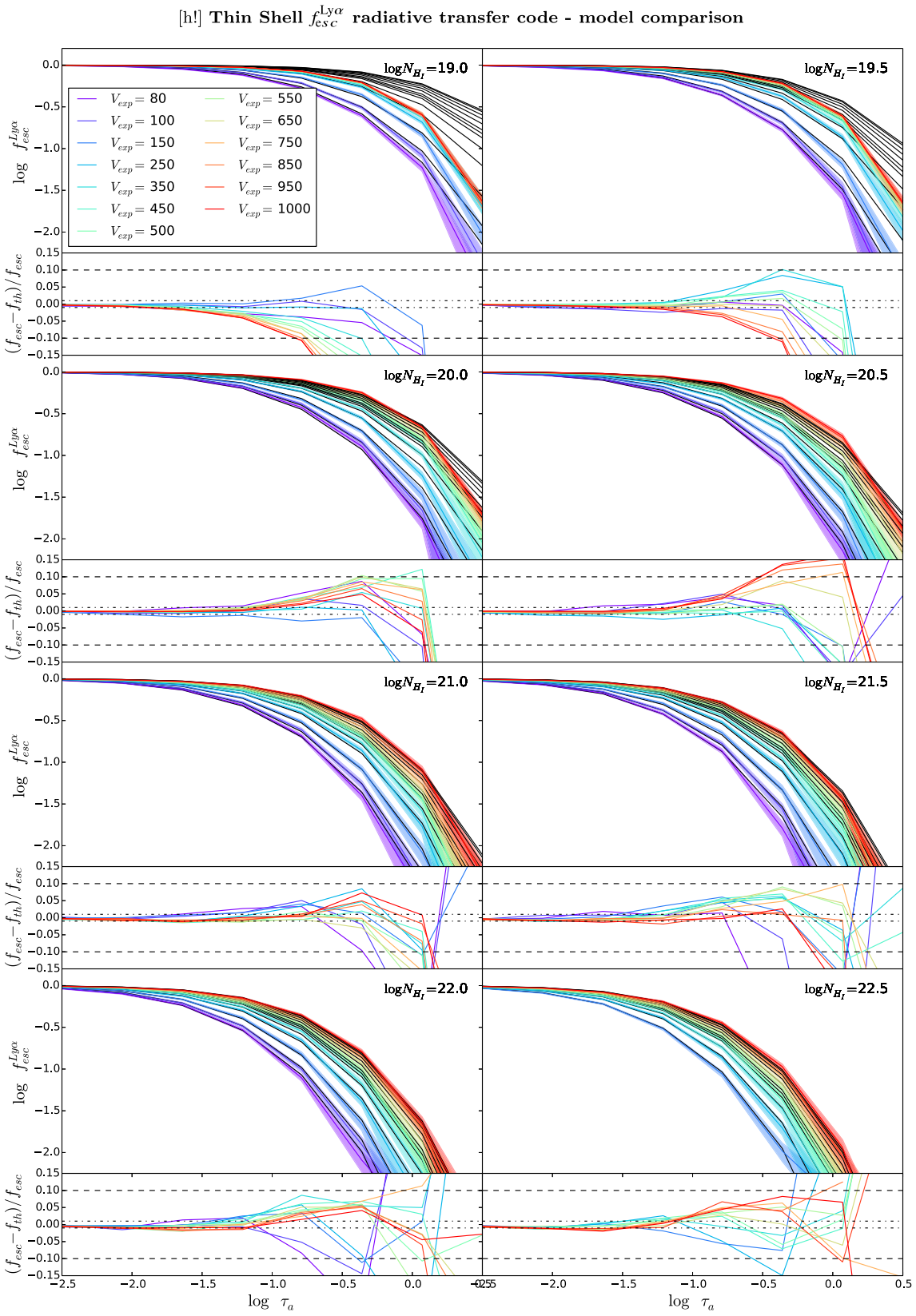

Figure B3. Comparison between the output of the radiative transfer code and our model for the $f_{\rm esc}^{Ly\alpha}$ in the *Thin Shell* geometry. Each panel is divided in top (the values of the escape fraction) and bottom (relative difference between our model and the radiative transfer code). In top panels the output from the radiative transfer code is plotted in colored lines (colour coded by the velocity of the system) with their errors (shades with the same colour) and our model prediction in black. In bottom panels the relative differences between our model and our code are plotted in colored lines and the ±1 per cent and ±10 per cent are represented by black dashed-dotted and dashed lines, respectively. Note that the colour code is the same in every panel.

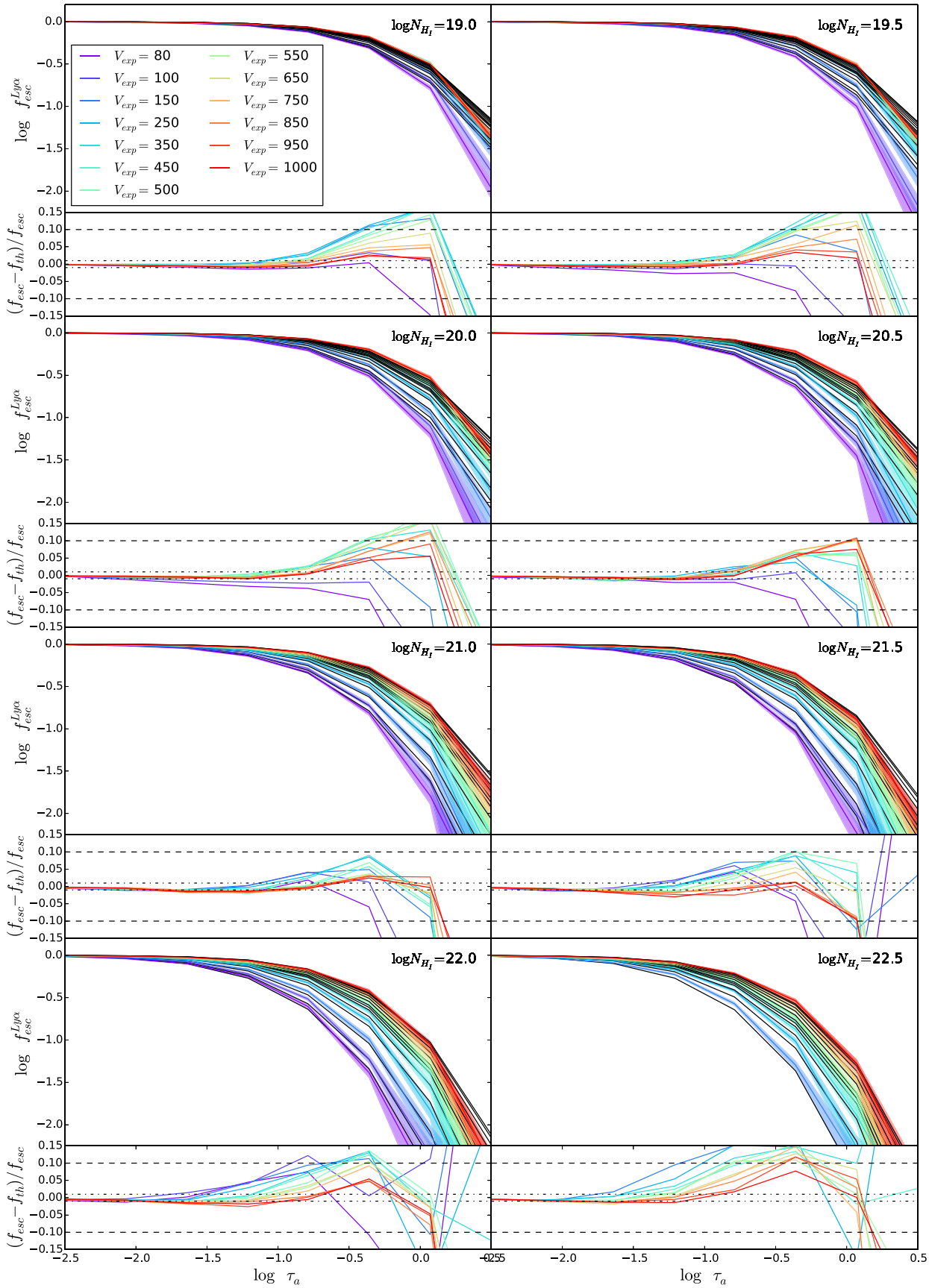

Figure B4. Same as fig. B4 but for the galactic wind.

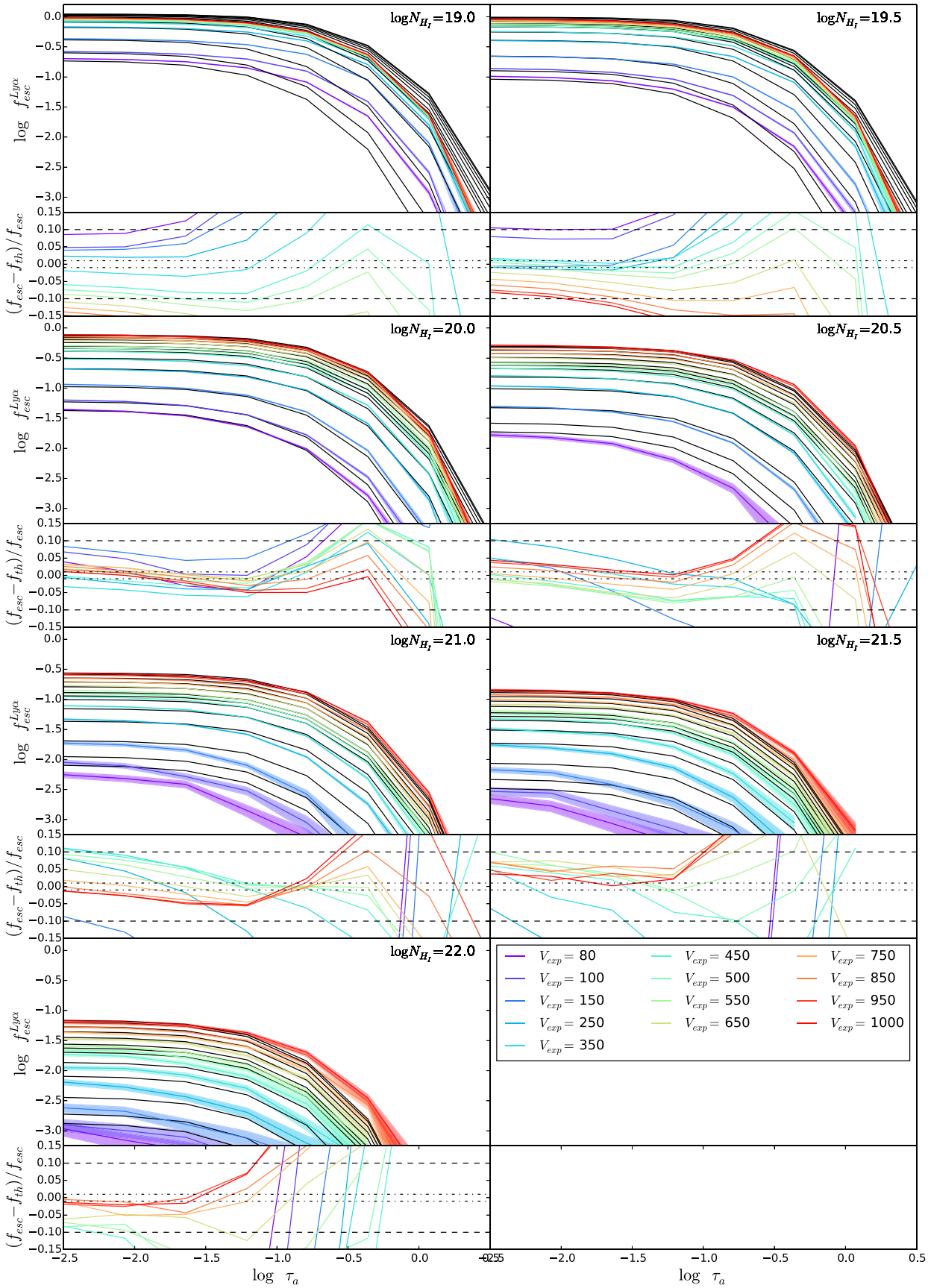

Figure B5. Same as fig. B5 but for the biconical galactic wind.

Table B1. Properties of the different mock catalogues and surveys.

Authors	z	$EW_{0,cut}$[Å]					$L_{Ly\alpha,cut}$ [erg s^{-1}]				
		Survey	Thin Shell	Wind	Bicone	AM	Survey	Thin Shell	Wind	Bicone	AM
Kusakabe et al. (2018)	2.2	20.0	19.91	20.3	18.79	19.52	1.62×10^{42}	1.54×10^{42}	1.92×10^{42}	1.38×10^{42}	1.6×10^{42}
Bielby et al. (2016)	3.0	65.0	42.0	48.37	46.05	20.42	1.62×10^{42}	1.33×10^{42}	1.57×10^{42}	1.47×10^{42}	1.48×10^{42}
Ouchi et al. (2018)	5.7	20.0	20.06	20.06	18.77	21.45	6.3×10^{42}	7.39×10^{42}	6.89×10^{42}	2.61×10^{42}	6.78×10^{42}
Ouchi et al. (2018)	6.7	20.0	20.06	20.06	15.88	21.45	7.9×10^{42}	7.7×10^{42}	6.11×10^{42}	1.86×10^{42}	8.37×10^{42}

et al. 2011; Konno et al. 2016; Sobral et al. 2017) and Kusakabe et al. (2018).

However, at $z = 3.0$ the selection criteria of the surveys used to fit the LF have different cuts in equivalent width (Cassata et al. 2011 $EW_{0,cut} = 20$ Å and Ouchi et al. 2008 $EW_{0,cut} = 64$ Å) while Bielby et al. (2016) (clustering measurements) have $EW_{0,cut} = 65$ Å.

The best scenario happens at redshifts 5.7 and 6.7, where the surveys used to calibrate our models (Ouchi et al. 2008; Konno et al. 2016), are practically the same in sky coverage and selection criteria than the ones used to constrain the clustering (Ouchi et al. 2010, 2018).

The second method to construct mock catalogues consists in matching the observed number density of sources. This can be achieved by relaxing the selection criteria. To minimize the possible secondary effects in the clustering due to changes in the selection criteria, we choose the combination that minimizes

$$Q = (\log L_{Ly\alpha,n} - \log L_{Ly\alpha,s})^2 + (\log EW_{0,n} - \log EW_{0,s})^2, \quad \text{(B1)}$$

where $L_{Ly\alpha,s}$ and $EW_{0,s}$ are the $L_{Ly\alpha,cut}$ and $EW_{0,cut}$ imposed by each survey and $L_{Ly\alpha,n}$ and $EW_{0,n}$ define the iso-n_{LAE} curve with the LAE observed abundance. In Table B1 we list $L_{Ly\alpha,s}$ and $EW_{0,s}$ for the different surveys and the used values of $L_{Ly\alpha,cut}$ and $EW_{0,cut}$ to construct the mock catalogues.

In Figs C1, C2, C3, and C4 we show the predicted n_{LAE} by our different models for several $L_{Ly\alpha,cut}$-$EW_{0,cut}$ combinations at $z = 2.2$, 3.0, 5.7, and 6.7, respectively. In these figures we also show $L_{Ly\alpha,cut}$ and $EW_{0,cut}$ of each of the surveys used for clustering in black dashed lines. The intersection between these shows the location of the clustering surveys selection criteria. Additionally, it is shown the individual value of n_{LAE} predicted by our models imposing the observational cuts (indicated with the white arrow). We also show the curve with constant n_{LAE} matching the observed abundance (solid black line). Finally, the $L_{Ly\alpha,cut}$-$EW_{0,cut}$ combination that minimizes equation (B1) is shown as a white dot.

At redshift 2.2 the predicted (using the survey selection criteria) and observed n_{LAE} match quite well. Thus, $L_{Ly\alpha,cut}$ and $EW_{0,cut}$ are very similar to $L_{Ly\alpha,s}$ and $EW_{0,s}$. However, the opposite case is found at $z = 3.0$, where predicted n_{LAE} is heavily underestimated in comparison with observations. This is mainly due to the mismatch between the predicted EW_0 distribution and the observed one. This might be due to the difference in selection criteria used the authors of the works for constraining the LF and the work building the clustering sample. While $L_{Ly\alpha,cut}$ is relatively similar to $L_{Ly\alpha,s}$, in order to recover the observed n_{LAE}, in all models, the value of $EW_{0,cut}$ is significantly lower than that of $EW_{0,s}$.

The scenarios at redshifts 5.7 and 6.7 are quite similar. At both redshifts the predicted number density, using the survey selection criteria, and observed n_{LAE} match quite well for the *Thin Shell*, *Wind*, and AM-noRT samples. However, in the *Bicone* model, $L_{Ly\alpha,cut}$ and $L_{Ly\alpha,s}$ are very different. In particular, the *Bicone* model requires a low $L_{Ly\alpha,cut}$ in order to balance underestimation of abundance (see Fig. 3).

APPENDIX C: CHOOSING AN EW AND LUMINOSITY CUT FOR THE MOCK CATALOGUES

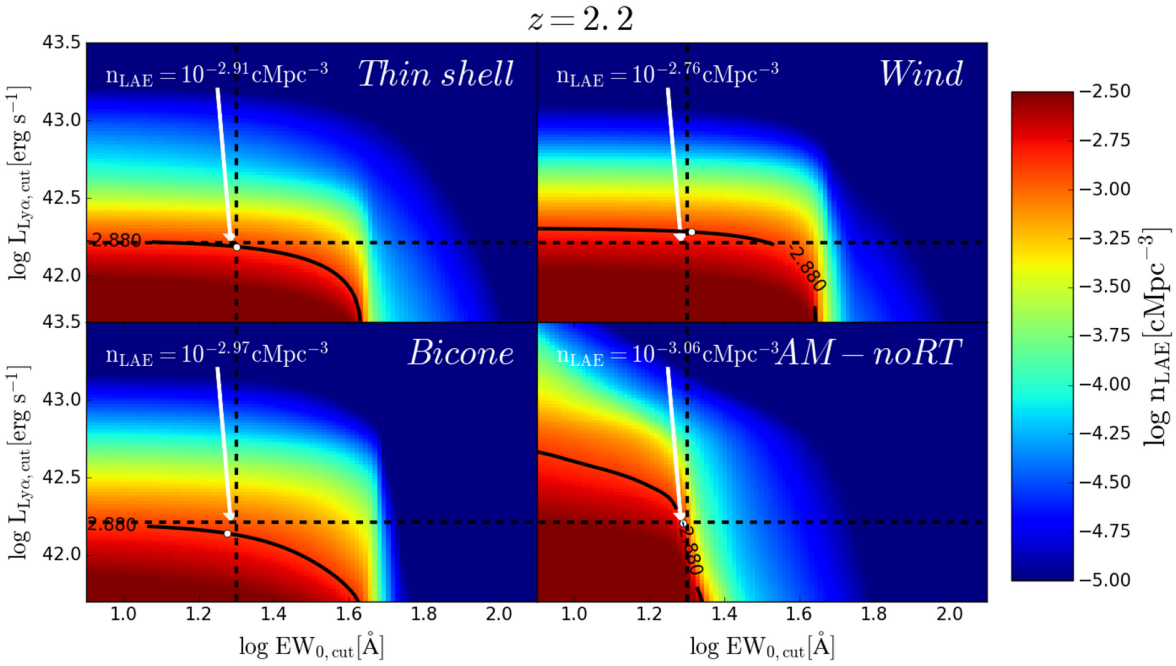

[h!]

Figure C1. Number density of LAEs n_{LAE} with Lyα luminosity $L_{Ly\alpha} > L_{Ly\alpha,cut}$ and Lyα rest frame equivalent width $EW_0 > EW_{0,cut}$ at redshift 2.2 for the *Thin Shell* (top left), *Wind* (top right), *Bicone* (bottom left), and AM-noRT (bottom right) model. In horizontal and vertical dashed black line we show the cut in $L_{Ly\alpha}$ and EW_0, respectively, in the survey at this redshift (Kusakabe et al. 2018). The place where these lines intersect sets the predicted n_{LAE} by our models which value is indicated in the same panel. The solid back line is the iso-number density curve of the observed n_{LAE}. The white dot indicates the position in the iso-number density curve that minimizes the distance between our model prediction and the observed n_{LAE}. .

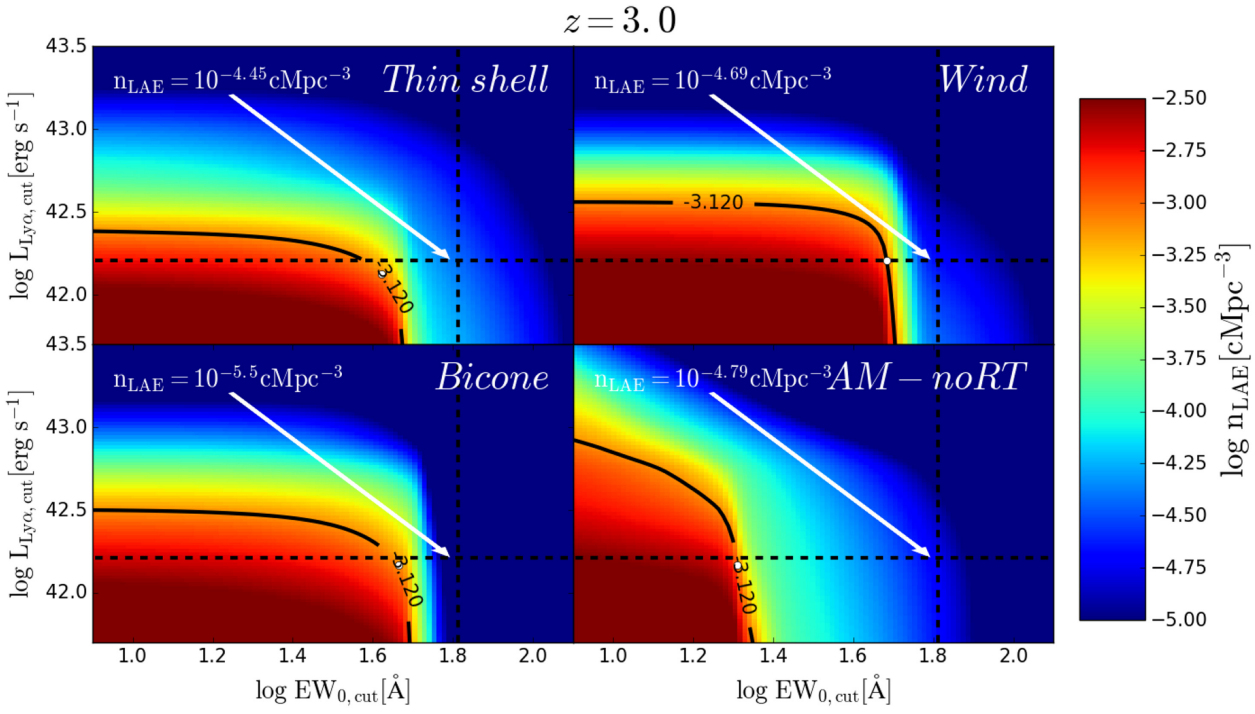

Figure C2. Same as Fig. C1 but at redshift 3.0 (Bielby et al. 2016).

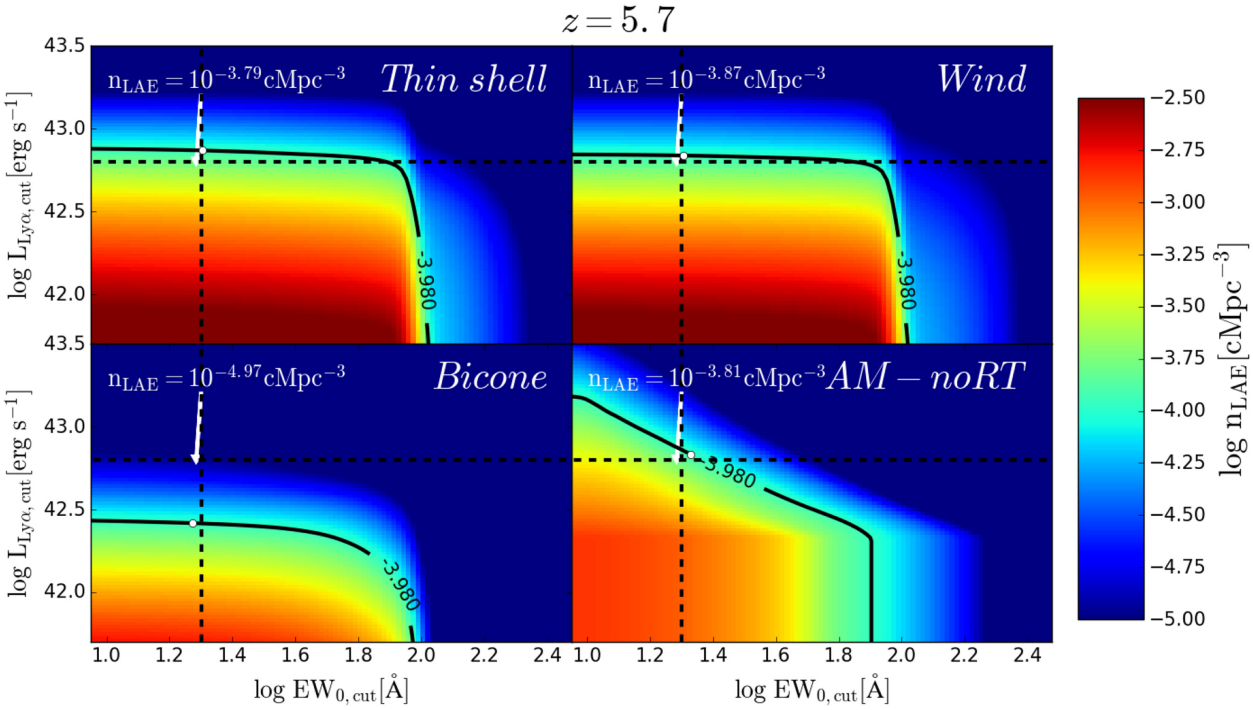

Figure C3. Same as Fig. C1 but at redshift 5.7 (Ouchi et al. 2018).

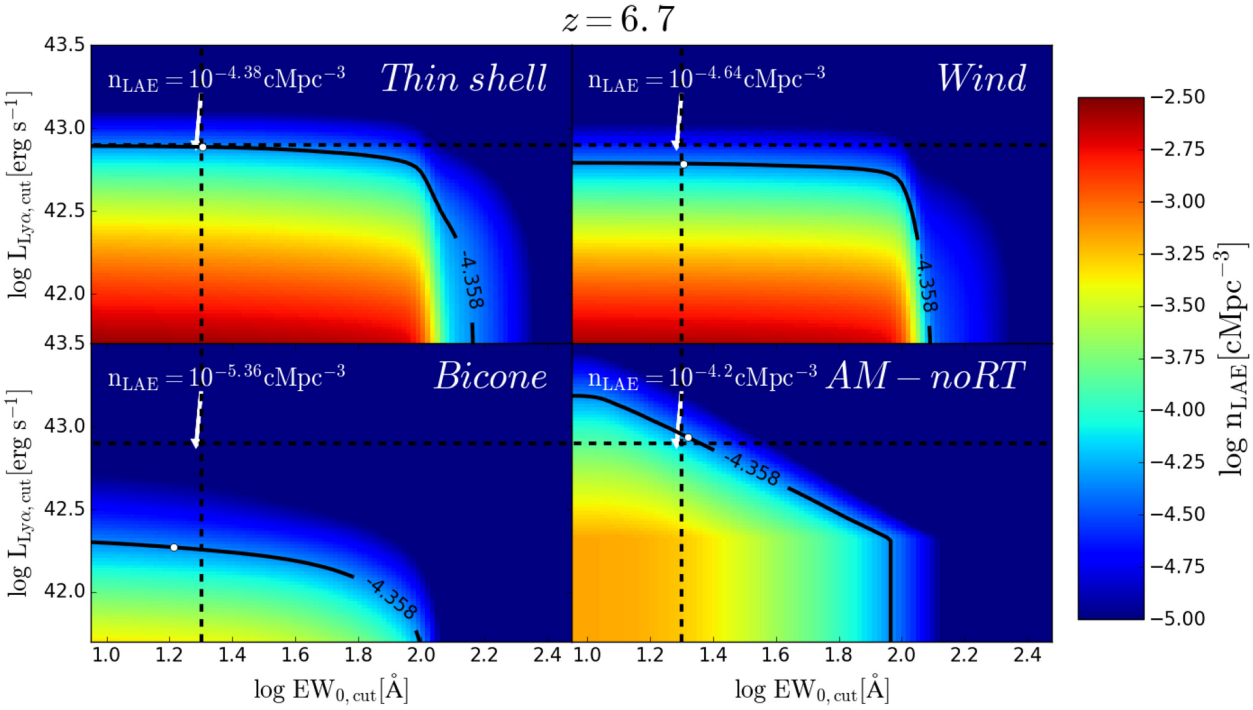

Figure C4. Same as Fig. C1 but at redshift 6.7 (Ouchi et al. 2018).

This paper has been typeset from a TEX/LATEX file prepared by the author.